# Three-dimensional numerical simulation of vesicle dynamics using a front-tracking method

Alireza Yazdani and Prosenjit Bagchi*
*Department of Mechanical & Aerospace Engineering, Rutgers University, the State University of New Jersey, Piscataway, New Jersey 08854, USA*
(Received 29 December 2011; published 22 May 2012)

Three-dimensional numerical simulation using the front-tracking method is presented on the dynamics of a vesicle in a linear shear flow. The focus here is to elucidate the parametric dependence and the self-similarity of the vesicle dynamics, quantification of vesicle deformation, and the analysis of shape dynamics. A detailed comparison of the numerical results is made with various theoretical models and experiments. It is found that the applicability of the theoretical models is limited despite some general agreement with the simulations and experiments. The deviations between the perturbative results and the simulation results occur even in the absence of thermal noise. Specifically, we find that the vesicle dynamics does not follow a self-similar behavior in a two-parameter phase space, as proposed in a theoretical model. Rather, the dynamics is governed by three controlling parameters, namely, the excess area, viscosity ratio, and dimensionless shear rate. Additionally, we find that a linear scaling of the tank-treading angle, as proposed in the theoretical model, is possible only for nearly spherical vesicles. The breakdown of the scaling occurs at higher values of the excess area even in the absence of thermal noise. We find that the vesicle deformation saturates at large shear rates, and the asymptotic deformation matches well with a theoretical prediction for nearly spherical vesicles. The dependence of the critical viscosity ratio associated with the onset of unsteady dynamics on the vesicle excess area is in excellent agreement with the experimental observation. We show that near the transition between the tank-treading and tumbling dynamics, both the vacillating-breathing-like motion characterized by a smooth ellipsoidal shape and the trembling-like motion characterized by a highly deformed shape are possible. For the trembling-like motion, the shape is highly three-dimensional with concavities and lobes, and the vesicle deforms more in the vorticity direction than in the shear plane. A Fourier spectral analysis of the vesicle shape shows the presence of the odd harmonics and higher order modes beyond fourth order.

DOI: 10.1103/PhysRevE.85.056308 PACS number(s): 47.63.−b, 87.85.gf, 47.15.G−

## I. INTRODUCTION

Vesicles are viscous liquid drops enclosed by membranes of lipid bilayers. They are often considered as the model particles for the human red blood cells. The bilayer membrane has two unique characteristics: It behaves as a two-dimensional incompressible fluid, and exhibits a bending resistance. Because of the interior fluid, and the liquid nature of the membrane, vesicles are highly deformable. Vesicles are also present in other eukaryotic cells where they form by membrane budding and pinching and act as the intracellular transport vehicles. Synthetic vesicles (liposomes) can be used as drug carriers for targeted delivery. Because of their biological and engineering applications, the dynamics of vesicles in flow has received significant attention in recent years.

When placed in a linear shear flow, a single vesicle undergoes primarily two types of motion: a steady tank-treading motion (hereafter referred to as TT) in which it aligns at a fixed angle with the flow direction while the membrane and the interior fluid execute a rotary motion, and an unsteady tumbling motion (hereafter referred to as TU) in which it flips like a rigid body. If deformation is neglected, the vesicle dynamics is controlled by two parameters: the excess area $\Delta = A/a_o^2 - 4\pi$ and the viscosity ratio $\lambda = \mu_i/\mu_o$, where $A$ is the surface area, $a_o$ is the radius of a sphere having the same volume, and $\mu_i$ and $\mu_o$ are the dynamic viscosities of the interior and exterior fluids, respectively. In this limit, the dynamics can be described by the theory of Keller & Skalak [1]. For a given excess area, the tank-treading motion occurs when the the viscosity ratio $\lambda$ is less than a critical value $\lambda_c$, and tumbling motion occurs when $\lambda > \lambda_c$.

When deformation is considered, a third controlling parameter, namely, the capillary number, or the dimensionless shear rate, $\chi = \mu_o \dot{\gamma} a_o^3/E_b$, also arises, where $E_b$ is the membrane bending modulus, and $\dot{\gamma}$ is the shear rate. Vesicle deformation can occur in tumbling as well as tank-treading motion. The role of deformation, however, becomes most important in trembling [2–4], vacillating-breathing [5–7], and swinging [8] motions, which are new types of unsteady motion that have been observed recently. In such motions, the inclination angle oscillates about the flow direction while the vesicle may undergo a periodic shape deformation. While differences exist between the trembling, vacillating-breathing, and swinging modes, particularly because they were observed or predicted by different tools, experimental, numerical, or analytical, one common feature is that they occur in the vicinity of the transition between the TT and TU modes. Hereafter, we refer to these new modes as the transition (TR) mode. Phase diagrams in the $\chi$-$\lambda$ plane, which depend on $\Delta$, can be used to describe the transition from one mode to the other. For small values of $\chi$, the transition occurs directly from TT to TU with increasing $\lambda$. For $\chi \gtrsim 1$, the transition occurs as TT to TR to TU with increasing $\lambda$. Complex and highly convoluted shapes of trembling vesicles, in the form of membrane budding and pinching, have been observed in experiments [3,9,10].

The role of the controlling parameters, particularly, the capillary number $\chi$, has received significant attention in recent

*Corresponding author: pbagchi@jove.rutgers.edu

 ©2012 American Physical Society

years. Numerous theoretical studies have been carried out, starting with Seifert [11], in the framework of perturbation analysis of nearly spherical vesicles ($\Delta \ll 1$) in which the shape is represented by a series of spherical harmonics, and the vesicle dynamics is expressed in terms of two coupled ODEs. In the leading-order analysis of Misbah [5] and Vlahovska & Gracia [12], the $\chi$-dependent terms drop out from the expansion, and the parametric space is reduced to two variables, namely, $\Delta$ and $\lambda$. Danker *et al*. [6], Kaoui *et al*. [7], and Lebedev *et al*. [4,13] considered the second-order terms in the expansion and up to the second harmonics, and thus retained the $\chi$ dependence. Lebedev *et al*. [4,13] showed that the parametric space could still be reduced by introducing two new dimensionless variables $S$ and $\Lambda$ defined as

$$S = \frac{7\pi}{3\sqrt{3}} \frac{\chi}{\Delta} \tag{1}$$

and

$$\Lambda = \frac{23\lambda + 32}{8\sqrt{30\pi}} \sqrt{\Delta}\,. \tag{2}$$

Using these two parameters, a self-similar behavior of the vesicle dynamics was obtained; that is, the transition boundaries between different regimes in the $S$-$\Lambda$ plane were found to be independent of $\Delta$. Experimental works by Steinberg's group [3] and a recent analysis of their data by Zabusky *et al*. [2] tend to suggest that the data can be presented in the two-parameter phase diagram proposed by Lebedev *et al*. [4,13] within the margin of uncertainty in the experiments, despite the fact that the experimental observations did not support some key assumptions in the models. In addition to the fact that the models are strictly applicable to nearly spherical vesicles, they are also based on the assumptions that the thermal fluctuations (except Seifert's [11]) and the odd harmonics in the vesicle shape are neglected.

The notion of self-similarity in vesicle dynamics, however, remains an issue of recent debate. In contrast to the model of Lebedev *et al*. [4,13], the models of Danker *et al*. [6] and Kaoui *et al*. [7] found that the self-similar solution did not exist, and the dynamics explicitly depended on the three parameters, $\chi$,$\lambda$, and $\Delta$. Farutin, Biben, & Misbah [14] included the fourth-order harmonics in the expansion, resulting in a 14-ODE model, and also found the absence of the self-similarity. Very recently, Biben, Farutin, & Misbah [15] used a 3D boundary integral simulation to study vesicle dynamics in shear flow and concluded that the self-similarity did not exist. Using the self-similarity model, Zabusky *et al*. [2] showed that all experimental tank-treading angles $\theta$ for different $\Delta$ collapsed to a single line when plotted against $\Lambda$ (excluding the data points which are presumed to be affected by thermal noise). Further, the boundary integral simulations of Kraus *et al*. [16] predicted that the tank-treading angle was independent of $\chi$. In contrast, all higher order theoretical models found an explicit dependence of $\theta$ on $\chi$.

The above discussion clearly suggests that further analysis is necessary with regard to the parametric space that controls the vesicle dynamics, without the limitation imposed by the assumption of the quasisphericity, in particular. The first objective of this article is to provide further insight to the parametric dependence and the self-similar behavior of the vesicle dynamics in the range of $\Delta = O(1)$ using a three-dimensional direct numerical simulation in which vesicle deformation is fully resolved but thermal noise is neglected.

Quantitative data on vesicle deformation is relatively scarce. The vesicle shape changes from its initial shape under the application of the shear, while the volume and surface area remain constants. In their experiments, de Haas *et al*. [17] observed that deformation increased nonlinearly with increasing shear rate and tend to saturate at large values. Seifert's theoretical work [11], which included thermal noise, predicted a linear behavior in the limit of vanishingly small shear rate, and a deformation saturation at large shear rates similar to that observed by de Haas *et al*. [17]. Kantsler & Steinberg [18] also observed a similar crossover behavior and saturation of deformation at large shear rate. Here, we present a quantitative comparison of the theoretical and experimental results with our 3D simulation results.

Another objective of this article is to analyze the shape dynamics for vesicles in the transition regime. As mentioned above, highly convoluted shapes are observed for the trembling vesicles in the experiments. These shapes are drastically different from those predicted for the vacillating-breathing vesicles by Danker *et al*. [6] in which the vesicle shape remains nearly elliptical during its oscillation. In this article, we show that our simulations are able to predict that in the absence of thermal noise, both the vacillating-breathing mode characterized by relatively smooth elliptical shapes, as well as the trembling mode characterized by complex shapes with concave regions, are possible.

Because of the role of deformation and higher order modes, a fully resolved numerical approach is deemed necessary in the analysis of vesicle dynamics. Several numerical methods have been developed to date: the boundary integral methods of Kraus *et al*. [16] and Biben, Farutin, & Misbah [15]; the phase field approach of Biben, Kassner, & Misbah [19]; 2D simulations of Ghigliotti, Biben, & Misbah [20]; simulations using multiparticle collision dynamics by Noguchi & Gompper [8,21] and Messlinger *et al*. [22]; spectral boundary integral simulations of Zhao & Shaqfeh [23]; and the boundary integral method of Veerapaneni *et al*. [24,25], to name a few. Here we present a 3D simulation using the front-tracking method. The article is organized as follows: In the next section the numerical method and its validation are presented. Then we present a comprehensive analysis of the scaling of the tank-treading angle and deformation, followed by the analysis of vesicle shapes in the transition region and the phase diagrams.

## II. COMPUTATIONAL METHODOLOGY

Three-dimensional numerical simulations using the front-tracking method are considered for vesicles immersed in a linear shear flow $\mathbf{u}^{\infty} = \{\dot{\gamma} y, 0, 0\}$. The initial shape is taken to be a prolate spheroid with the axis of symmetry in the shear plane. The vesicle is represented as a liquid drop surrounded by a zero-thickness membrane. The interior and suspending fluids are assumed to be incompressible and Newtonian with viscosities $\lambda\mu_o$ and $\mu_o$, respectively. The membrane is assumed to possess the resistance against bending and area dilatation. The bending resistance is modeled following

Helfrich's [25] formulation for bending energy

$$W_b = \frac{E_b}{2}\int_S (2\kappa - c_o)^2\, dS + E_g \int_S \kappa_g dS, \tag{3}$$

where $E_b$ is the bending modulus associated with the mean curvature $\kappa$, $E_g$ is the bending modulus associated with the Gaussian curvature $\kappa_g$, $c_o$ is the spontaneous curvature, and $S$ is the vesicle surface area. According to the Gauss-Bonnet theorem of differential geometry the second integral in Eq. (3) remains invariant for topologically equivalent shapes. The surface force density can be derived by calculating the first variation of $W_b$. Then, the expression will involve both $\kappa$ and $\kappa_g$, but not $E_g$. The resistance against area dilatation gives rise to a local in-plane tension $\sigma$, and an associated energy $\int_S \sigma dS$. Thus, the total energy of the membrane becomes

$$W = \frac{E_b}{2}\int_S (2\kappa - c_o)^2\, dS + \int_S \sigma dS. \tag{4}$$

The membrane force density acting on the fluid as a reaction force becomes

$$\mathbf{f}_n = E_b[(2\kappa + c_o)(2\kappa^2 - 2\kappa_g - c_o\kappa) + 2\,\Delta_{LB}\,\kappa]\mathbf{n} - 2\sigma\kappa\,\mathbf{n}, \tag{5}$$

$$\mathbf{f}_t = \nabla_s \sigma, \tag{6}$$

where $\mathbf{n}$ is the unit vector that is normal to the vesicle surface and directing outward, $\nabla_s = \mathbf{I}_s \cdot \nabla$ is the surface gradient operator, $\Delta_{LB} = \nabla_s \cdot \nabla_s$ is the Laplace-Beltrami operator, and $\mathbf{I}_s = \mathbf{I} - \mathbf{nn}$ is the surface projection matrix [26]. Here $\mathbf{f}_n$ is the normal force, and $\mathbf{f}_t$ is the in-plane force arising due to the constraint of area dilatation. It should also be mentioned that based on our conventions a sphere will have a positive mean curvature.

The fluid motion inside and outside the vesicle is governed by the continuity and Navier-Stokes equations

$$\nabla \cdot \mathbf{u} = 0, \tag{7}$$

$$\rho\left[\frac{\partial \mathbf{u}}{\partial t} + \mathbf{u}\cdot\nabla\mathbf{u}\right] = -\nabla p + \nabla\cdot\mu[\nabla\mathbf{u} + (\nabla\mathbf{u})^T]. \tag{8}$$

The membrane and the fluid are coupled in a two-way manner by adding a source term to the right-hand side of (8) as

$$\mathbf{F} = \int_S (\mathbf{f}_n + \mathbf{f}_t)\ \delta(\mathbf{x} - \mathbf{x}')d\mathbf{x}', \tag{9}$$

where $\delta$ is the three-dimensional Dirac-Delta function, $\mathbf{x}'$ is a location on the vesicle surface, and $\mathbf{x}$ is a location in the flow. Once the fluid velocity $\mathbf{u}(\mathbf{x},t)$ is known, the vesicle surface is advected as $d\mathbf{x}'/dt = \mathbf{u}_S$ where the surface velocity $\mathbf{u}_S$ is obtained by interpolating the local fluid velocity $\mathbf{u}$ using the delta function as

$$\mathbf{u}_S = \int_S \mathbf{u}(\mathbf{x})\delta(\mathbf{x} - \mathbf{x}')d\mathbf{x}. \tag{10}$$

The computational domain is a cubic box of length $2\pi a_o$ and contains one vesicle of equivalent radius $a_o$. The domain is periodic in the $x$ and $z$ directions and wall-bounded in the $y$ direction. The no-slip condition is imposed on the walls. The domain is discretized using a fixed (Eulerian) rectangular and uniform grid of $120^3$ points. For this resolution, there are about 38 Eulerian points across the diameter of the equivalent sphere. Thus the flow field inside the vesicle is well resolved. A smooth representation of the delta function spanning over four Eulerian points is used [27]. A combined second-order finite difference scheme and Fourier transform is used for the spatial discretization, and a second-order time-split scheme is used for the temporal discretization of the Navier-Stokes equations.

We now describe the numerical technique to compute the normal force $\mathbf{f}_n$. The vesicle surface is discretized using small flat triangular elements (Fig. 1). Typically, we use 5120 triangular elements, or 2562 Lagrangian nodes or vertices. Each vertex is surrounded by five or six elements. The curvatures $\kappa$ and $\kappa_g$ on the triangulated surface is calculated by a quadratic surface fitting,

$$z' = ax'^2 + bx'y' + cy'^2 + dx' + ey', \tag{11}$$

where $(x',y',z')$ is a local coordinate system with origin at a Lagrangian point of interest, and the coordinate $z'$ is aligned with the estimated normal vector. The technique of computing the curvatures and their derivatives is described in detail by Garimella & Swartz [28] and Petitjean [29]. One-ring neighbor points are used to find the coefficients using a least-square method, and iterations are performed to obtain an accurate fitting until a satisfactory convergence for the estimated normal vector is reached. The curvatures, $\kappa$ and $\kappa_g$, are expressed in terms of the fitted coefficients as

$$\kappa = -\frac{a + c + ae^2 + cd^2 - bde}{(1 + d^2 + e^2)^{3/2}} \tag{12}$$

and

$$\kappa_g = \frac{4ac - b^2}{(1 + d^2 + e^2)^2}\,. \tag{13}$$

To discretize the Laplace-Beltrami operator, we work in the framework of computational image reconstruction [30,31]. For a Lagrangian node $\mathbf{x}'_i$, the Laplace-Beltrami operator is written as

$$\Delta_{LB}\,\kappa_i = \frac{1}{2\mathcal{A}}\sum_{j\in N_1(i)} \tilde{\mathbf{n}}_j \cdot (\nabla_s\kappa_j + \nabla_s\kappa_{j+})\|\mathbf{x}'_j - \mathbf{x}'_{j+}\|, \tag{14}$$

where $N_1(i)$ represents the set of vertices in the first ring neighborhood of $i$ [see Fig. 1(b)], $\tilde{\mathbf{n}}_j$ is the unit outward normal to the edge $[j, j+]$, and $\mathcal{A}$ is the area of all triangles sharing the node $i$. Further, the gradient $\nabla_s\kappa_i$ at a node $i$ is approximated by a weighted average of the gradients on the adjacent triangles as

$$\nabla_s\kappa_i = \frac{1}{\mathcal{A}}\sum_{j\in N_1(i)} A_j \nabla_{T_j}\kappa, \tag{15}$$

where $\nabla_{T_j}\kappa$ is the surface gradient approximation of the mean curvature on each adjacent triangle $T_j = [i, j, j+]$, and $A_j$ is the area of $T_j$. Assuming that $\kappa$ varies linearly in each triangle,

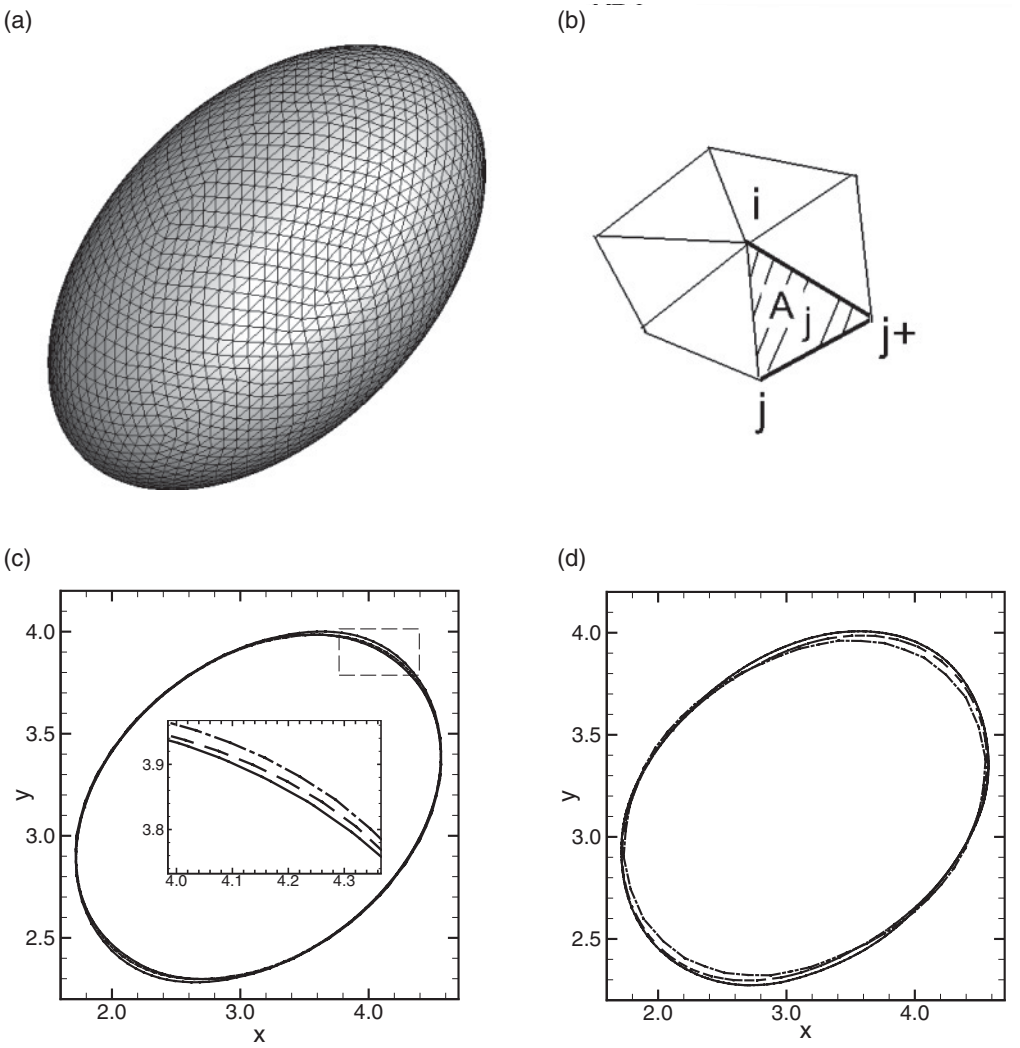


FIG. 1. (a) Discretization of the vesicle surface. (b) Schematic for the first-ring neighbors of the vertex $i$. (c) Convergence test of Eulerian resolution: solid line, $80^3$; dashed line, $120^3$; dot-dashed line, $160^3$. The inset shows a magnified view of a part of the contours. (d) Convergence test of Lagrangian resolution: dot-dashed line, 1280; dashed line, 5120; solid line, 20480 triangles.

$\nabla_{T_j}\kappa$ can be written as

$$\begin{aligned}\nabla_{T_j}\kappa = \frac{1}{4A_j^2}\{&\kappa_i[(\mathbf{x}_i' - \mathbf{x}_j')\cdot(\mathbf{x}_j' - \mathbf{x}_{j+}')(\mathbf{x}_{j+}' - \mathbf{x}_i') \\ &+ (\mathbf{x}_i' - \mathbf{x}_{j+}')\cdot(\mathbf{x}_{j+}' - \mathbf{x}_j')(\mathbf{x}_j' - \mathbf{x}_i')] \\ &+ \text{similar terms with } i \text{ and } j \text{ interchanged} \\ &+ \text{similar terms with } i \text{ and } j_+ \text{ interchanged}\}. \quad (16)\end{aligned}$$

The in-plane force $\mathbf{f}_t$ is computed by invoking a strain energy function for the membrane following the work of Skalak *et al*. [32] as

$$W_a = E_a\left(\epsilon_1^2\epsilon_2^2 - 1\right)^2, \quad (17)$$

where $\epsilon_1$ and $\epsilon_2$ are local principal stretch ratios, and $E_a$, which has the dimension of energy per unit area, is large enough to ensure a strong resistance against area dilatation. The detailed method of calculating $\mathbf{f}_t$ has been described in our earlier publications (e.g., [33]). Here we present a brief description for the purpose of completeness. The force in each triangular element on the vesicle surface is obtained from $W_a$ by applying the principle of virtual work as

$$\mathbf{f}_t^p = -\frac{\partial W_a}{\partial \mathbf{v}}, \quad (18)$$

where $\mathbf{v}$ is the displacement. The principal in-plane stretch ratios can be expressed in terms of the displacement gradient tensor $\mathbf{D}$ as

$$\epsilon_i^2 = \tfrac{1}{2}\left[G_{11} + G_{22} \pm \sqrt{\{(G_{11} - G_{22})^2 + 4G_{12}^2\}}\right], \quad i = 1,2, \quad (19)$$

where $\mathbf{G} = \mathbf{D}^{\mathrm{T}}\mathbf{D}$. A finite-element method is used to find the stretch ratios $\epsilon_1$, $\epsilon_2$, and $\mathbf{f}_t^p$ for each triangular element [34]. Then, the force $\mathbf{f}_t$ at each vertex is found as the resultant of $\mathbf{f}_t^p$ on the triangles surrounding the vertex. We note that (17) and (6) are not specifically related to each other. The former was derived by Skalak *et al*. for red blood cell membranes, which behave as a nearly incompressible surface. Hence, (18) is more convenient to use in the context of the front-tracking method as the Lagrange multiplier $\sigma$ is not needed. In applying the

virtual work principle, the membrane elements are considered to remain planar during the course of deformation, and hence the forces remain in-plane.

We use the equivalent radius $a_o$ as the length scale and the inverse shear rate $\dot{\gamma}^{-1}$ as the time scale. The dimensionless time is denoted by $t^*$, and defined as $t\dot{\gamma}$. Three relevant dimensionless parameters of the problems are the excess area $\Delta$, the viscosity ratio $\lambda$, and the capillary number $\chi$ which are defined in Sec. I. In our simulations, $\Delta$ is varied from 0.12 to 2.17. The corresponding range of the reduced volume $V^* = (1 + \Delta/4\pi)^{-3/2}$ is 0.99 to 0.79. This range is chosen primarily for two reasons: First, the theoretical results with which comparisons are made are valid for low values of the excess area only, and second, the experimental data with which comparisons are made are for $\Delta < 2.5$. The numerical method is able to handle lower reduced volumes than what is considered here. Using the same methodology, we have considered dynamics of red blood cells in shear flow for which the reduced volume is about 0.64 [35]. The only probable numerical limitation to considering even lower values of the reduced volume is that very fine mesh is needed to resolve the vesicle surface. The viscosity ratio $\lambda$ and the capillary number $\chi$ are varied from 1 to 14, and 0.2 to 50, respectively. The nonlinear terms in the Navier-Stokes equations are retained in the computation; however, the Reynolds number $\mathrm{Re} = \rho\, a_o^2\, \dot{\gamma}/\mu_o \approx 10^{-2}$, and hence the effect of inertia is negligible. The time integration scheme in our numerical technique is based on the second-order Adams-Bashforth explicit method for the convective terms and membrane forces and the semi-implicit Crank-Nicolson method for the viscous terms. Since the bending forces depend on the second-order derivatives of curvature, the system could become stiff for very small values of $\chi$; such cases are not considered here as thermal fluctuations may also be important then. Moreover, in the front-tracking method, the membrane force is distributed smoothly over 4 Eulerian grid points surrounding the Lagrangian point to avoid numerical instability. The integration time step is $\Delta t^* \sim 10^{-4}$, and is set by the area incompressibility condition, which appears to be more stringent than the bending stiffness.

Figures 1(c) and 1(d) present the convergence tests for the Eulerian and Lagrangian resolutions, respectively. Figure 1(c) shows the two-dimensional contours of the steady-state shape of a tank-treading vesicle in the shear plane for three different Eulerian grids: $80^3$, $120^3$, and $160^3$, while the Lagrangian resolution is kept constant at 5120 triangles. No significant difference is observed between the three cases, and thus $120^3$ resolution is used in this study. Figure 1(d) shows the result for three different Lagrangian resolutions: 1280, 5120, and 20480 triangles, while the Eulerian resolution is fixed at $120^3$. The result for 1280 elements is slightly different from the other two, whereas 5120 and 20480 resolutions give almost the same shapes. Tables I and II present the deformation parameter and inclination angle for different Eulerian and Lagrangian resolutions, which confirm that convergence is attained for $120^3$ mesh.

In order to verify the accuracy of the surface fitting method used to obtain the curvatures and their discrete gradients, we compare the numerically obtained values with the exact (analytical) values for a fixed oblate spheroid with an excess area $\Delta = 1.62$. The normalized $\mathcal{L}_2$ error is defined as

TABLE I. Convergence of deformation parameter $D$ and tank-treading inclination angle $\theta/\pi$ for different Eulerian resolutions. The Lagrangian grid is fixed at 5120 elements. Here $\Delta = 0.63$, $\lambda = 5$, $\chi = 50$.

| No. of Points | $D$ | $\theta/\pi$ |
|---|---|---|
| $40^3$ | 0.265 | 0.094 |
| $80^3$ | 0.298 | 0.080 |
| $120^3$ | 0.299 | 0.077 |
| $160^3$ | 0.299 | 0.077 |

$\mathcal{L}_2 = ||\mathbf{V} - \hat{\mathbf{V}}||_2/\|\mathbf{V}\|_2$, where $\mathbf{V}$ and $\hat{\mathbf{V}}$ represent the exact and numerical solutions, respectively. Table III presents the $\mathcal{L}_2$ error for $\kappa$, $\kappa_g$, and $\Delta_{LB}\kappa$. The $\mathcal{L}_\infty$ error which is the maximum relative error between the numerical and exact values is also given in Table IV. Values in Table III show that the $\mathcal{L}_2$ error can be significantly improved by increasing the number of elements from 1280 to 5120, while only a marginal improvement occurs when the number of elements is further increased to 20480. The same trend can be noticed for $\mathcal{L}_\infty$ error of $\kappa$ and $\kappa_g$. One exception is the $\mathcal{L}_\infty$ error in $\Delta_{LB}\kappa$ which first decreases as the number of elements increases from 1280 to 5120, but increases thereafter. It is mentioned in Ref. [31] that the convergence of the Laplace-Beltrami operator depends on the mesh structure, and hence, a uniform reduction in $\mathcal{L}_\infty$ error can be achieved for some specific triangulations only. It was noted in Fig. 1(d) that the vesicle shape does not show a significant change when the Lagrangian resolution is increased from 5120 to 20480. Hence, the mesh with 5120 elements was used in the simulations of the tank-treading and tumbling vesicles for which the shape is found to be smooth. For vesicles near the transition boundary, which show highly complex shapes, it was necessary to use the higher Lagrangian resolution. Our numerical scheme for the calculation of curvatures and their discrete gradients is robust for any smooth surfaces regardless of the shape; e.g., in Ref. [35], we considered dynamics of red blood cells for which the initial shape is a biconcave discoid, which was observed to evolve into more complex shapes than those reported here for vesicles.

A series of tests are performed to set an appropriate value of the prefactor $E_a$ in Eq. (17). It is found that for the dimensionless value of $\sim 10^3$, the vesicle surface area is conserved within 0.4% globally and locally. Further, because of the area constraint, a nearly spherical vesicle may deform by losing its volume. Such volume loss is observed in our simulation for lower values of $\Delta$ only, typically $<0.5$. In such cases, we find that the tank-treading inclination angle is rather sensitive to a small change in volume. The volume loss is

TABLE II. Convergence of deformation parameter $D$ and tank-treading inclination angle $\theta/\pi$ for different Lagrangian resolutions. The Eulerian grid is fixed at $120^3$. Here $\Delta = 0.63$, $\lambda = 5$, $\chi = 50$.

| No. of Elements | $D$ | $\theta/\pi$ |
|---|---|---|
| 1280 | 0.298 | 0.071 |
| 5120 | 0.299 | 0.077 |
| 20480 | 0.293 | 0.081 |

TABLE III. Normalized $\mathcal{L}_2$ error for different Lagrangian resolutions. The shape is an oblate spheroid with $\Delta = 1.62$.

| No. of Elements | $\kappa$ | $\kappa_g$ | $\Delta_{LB}\kappa$ |
|---|---|---|---|
| 1280 | 0.010 | 0.017 | 0.303 |
| 5120 | 0.003 | 0.005 | 0.108 |
| 20480 | 0.001 | 0.002 | 0.059 |

prevented by adding a uniform force

$$\mathbf{f}_v = -K_v \frac{\Delta V}{V_0}\mathbf{n}, \tag{20}$$

where $V_0$ is the initial volume, $\Delta V = (V - V_0)$ is the change, and $K_v$ is a sufficiently large positive number [36]. While the method has been applied for red blood cells in vacuum [36], we find it to be convenient and consistent within the framework of the immersed-boundary method for fluid-filled vesicles as well, and it also assures that the no-slip condition on the vesicle surface is automatically satisfied as the surface velocity is obtained by interpolating the local fluid velocity. It may be noted that volume preservation could be alternatively performed by using a surface normal velocity. We have performed multiple simulations using this alternate method and found that both methods gave similar results; e.g., for $\chi = 10, \lambda = 1, \Delta = 0.44$, the force method gave $D = 0.257, \theta/\pi = 0.176$, and the velocity method gave $D = 0.256, \theta/\pi = 0.178$. Table V presents the volume change and the tank-treading angle $\theta$ for a sample case at a high capillary number over a range of the dimensionless values of $K_v$. We see that from $K_v = 2.5 \times 10^4$ to $4 \times 10^4$, there is no significant improvement in volume and $\theta$. After careful tests, we find that $K_v = 2.5 \times 10^4$ is satisfactory for which the volume loss is about 0.12%. It should be emphasized that the volume loss is observed for the nearly spherical vesicles ($\Delta < 0.5$), and not for higher values of $\Delta$. Note that for higher values of $\Delta$, the surface area is higher, and hence, the distance between the Lagrangian nodes are also higher. However, this increased Lagrangian-to-Eulerian mesh size ratio did not cause any increased volume loss. We also observed that increasing the Lagrangian mesh from 1280 to 5120 and 20480 never improved the volume loss for a fixed Eulerian grid spacing of $120^3$. This suggests that the volume loss in our simulations is not due to higher Lagrangian-to-Eulerian mesh size ratio. For vesicles near the transition boundary, which show highly complex shapes (Figs. 11 and 12), we use 20480 Lagrangian resolution for improved curvature estimation. Also, we do not observe local coarsening or entanglement of surface mesh over the length of the simulations; thus, no remeshing is done. Figure 1(a) shows the surface mesh on a deformed vesicle;

TABLE IV. Normalized $\mathcal{L}_\infty$ error for different Lagrangian resolutions. The shape is an oblate spheroid with $\Delta = 1.62$.

| No. of Elements | $\kappa$ | $\kappa_g$ | $\Delta_{LB}\kappa$ |
|---|---|---|---|
| 1280 | 0.019 | 0.030 | 0.360 |
| 5120 | 0.008 | 0.012 | 0.166 |
| 20480 | 0.005 | 0.009 | 0.321 |

TABLE V. Volume loss and cell inclination angle for different dimensionless values of $K_v$. Here, $\Delta = 0.44, \lambda = 5$, and $\chi = 50$. The tabulated values are taken at $t^* = 20$.

| $\mathbf{K_v}$ | $\theta/\pi$ | $\frac{\Delta V}{V_0}$ (%) |
|---|---|---|
| $5 \times 10^3$ | 0.14 | −0.43 |
| $2.5 \times 10^4$ | 0.148 | −0.12 |
| $4 \times 10^4$ | 0.149 | −0.07 |

no mesh skewness is seen here. For all reported runs, we have made similar checks that the mesh skewness does not appear. Further, in our earlier studies on capsules with no area constraint, we did not observe any significant volume loss [33,37]. No significant volume loss was found also in our study on the dynamics of red blood cells, which have highly oblate resting shape ($\Delta \sim 5$) and nearly constant surface area using the same numerical technique [35]. Thus, it is unlikely that the volume loss observed here is due to the way the area constraint is implemented. Instead, we believe that the constraint prevents the area change of surface triangles, and thus prevents mesh skewness.

We have verified that there is no significant effect on the vesicle dynamics due to confinement by increasing the wall-to-wall distance from $2\pi a_0$ to $3\pi a_0$ and $4\pi a_0$. The tank-treading angles decrease by at most 5%, and the deformation parameter $D$ increases by less than 1% upon increasing the size to $3\pi a_0$; no further changes in $\theta$ and $D$ occur upon further increase to $4\pi a_0$. We have also verified that the tumbling and swinging motions, and the transition borders are not affected by increasing the wall-to-wall distance.

## III. RESULTS

### A. Analysis of tank-treading vesicles

First we present the results for the tank-treading vesicles, and address the scaling issues related to the inclination angle. For the range of $\Delta$ considered here ($\Delta \leqslant 2.17$), only a prolate equilibrium shape is possible [38]. First, we verify that by starting with an initially oblate or prolate shapes, our numerical technique leads to the same final shape. This is illustrated in Figs. 2(a)–2(b), where the shape evolution is shown for a vesicle of an initially oblate shape at $\Delta = 0.88$. The final shape after the initial transience shows that the vesicle has assumed a prolate-like shape. A marker particle on the surface is tracked over time to show the tank-treading motion. Figure 2(c) shows the time evolution of the semimajor axis $L$, semiminor axis $B$, the half of the end-to-end length in the vorticity direction, $Z$, and the major-axis inclination angle $\theta$ for initially oblate and prolate shapes, but at the same value of $\Delta$. It is clear that both shapes reach the same final steady state as $L$, $B$, $Z$, and $\theta$ approach the same values.

#### 1. Dependence of θ versus Δ

The dependence of the tank-treading inclination angle $\theta$ (angle between the major axis and the flow direction $x$) on the excess area $\Delta$ is shown in Fig. 3. The simulation data are presented for a fixed value of the capillary number $\chi = 10$ in the figure, but different values of the viscosity ratio $\lambda$. The

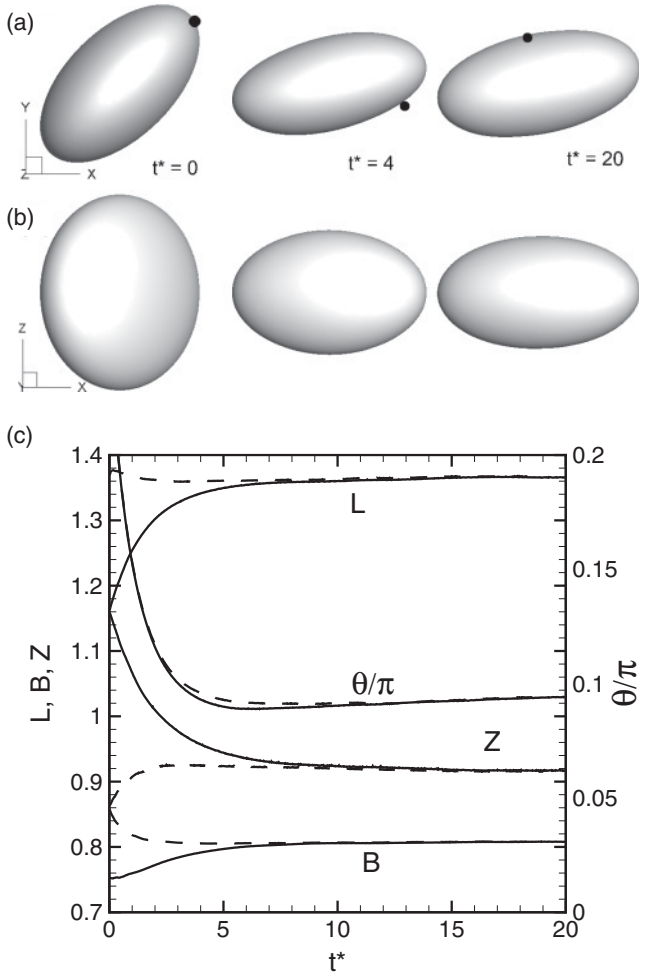


FIG. 2. Sample results on a tank-treading vesicle and oblate-to-prolate transition. (a) and (b) show the time-lapse shapes viewed along the vorticity direction and velocity gradient direction, respectively, for $\Delta = 0.88, \chi = 50, \lambda = 5$. A marker point (black dot) is shown in (a) to illustrate the membrane tank tread. (c) Time evolution of semimajor axis $L$, semiminor axis $B$, the half of the end-to-end length $Z$ in the vorticity direction, and the tank-treading angle $\theta$ for initially oblate (solid lines) and prolate (dashed lines) vesicles for $\Delta = 0.44, \chi = 50, \lambda = 5$. Both initial shapes lead to the same final results. All lengths are scaled by $a_o$.

present front-tracking simulation results are compared with the boundary integral simulation results of Kraus *et al*. [16] (who considered $\lambda = 1$ only), the recent spectral boundary integral simulations by Zhao & Shaqfeh [23] ($\lambda = 1$ and 2.7 from their simulations), and the experimental results of Steinberg and co-workers. The data points for the experimental results and the associated error bars are extracted from Fig. 4 in Zabusky *et al*. [2]. In general, the present results agree well with the experimental results and the earlier boundary integral simulations; however, certain subtle points must be mentioned. As noted in Refs. [2,3,9], each experimental data point represents an ensemble-averaged value over some bins of $\Delta$ obtained from more than 500 individual measurements. In the early measurements of Kantsler & Steinberg [9,18], the uncertainty of $a_o$, $\Delta$, and $\lambda$ was up to 20%. In the newer measurements of Deschamps *et al*. [3], the uncertainty of $a_o$ and $\Delta$ was 3.5%

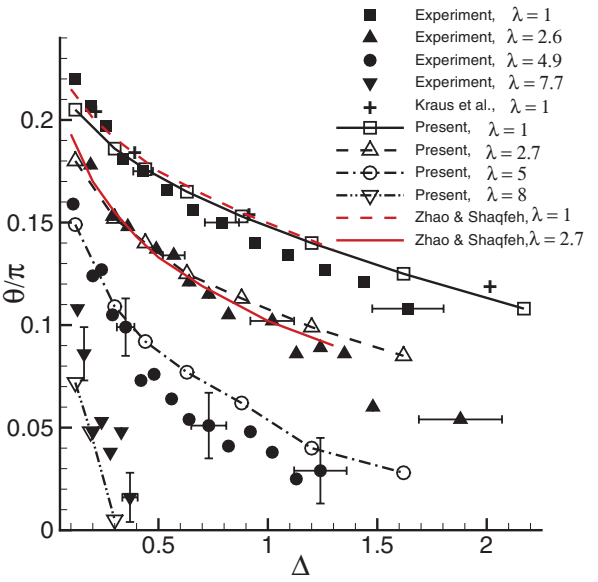


FIG. 3. (Color online) Effect of the excess area $\Delta$ on the inclination angle for tank-treading vesicles at different values of the viscosity ratio $\lambda$. Numerical results are shown by open symbols and lines, and for a fixed capillary number $\chi = 10$. Comparison is done with the experimental results (filled symbols) from Steinberg and co-workers, boundary integral simulations by Kraus *et al*. [16] (+), and spectral boundary integral simulations by Zhao & Shaqfeh [23]. The experimental data and the error bars are taken from Fig. 4 of Zabusky *et al*. [2].

and 16%, leading to the maximum errors of 25% and 8% in $S$ and $\Lambda$, respectively, though the inclination angle uncertainty was not reported. Given the error bars of the experimental data, we can conclude that there are very good agreements between the present results and the experimental data.

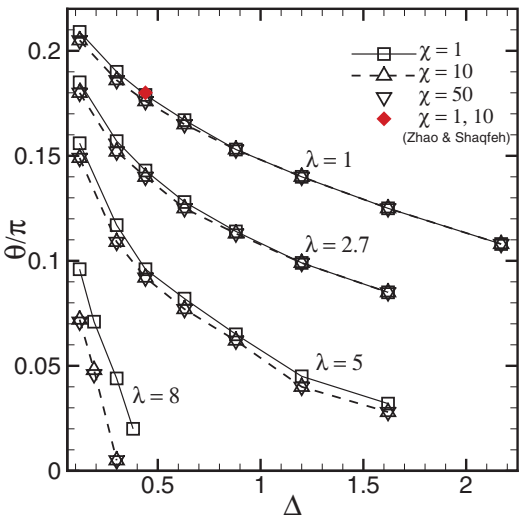


FIG. 4. (Color online) Simulation results showing the effect of $\chi$ on the $\theta$ vs $\Delta$ plot. For each value of $\lambda$, from 1 to 8, three values of $\chi$ are considered. The numerical results show a $\chi$ dependence at $\lambda = 5$ and 8. The red diamonds are data from Zhao & Shaqfeh [23] for $\lambda = 1$, $\Delta = 0.44$, and $\chi = 1$ and 10.

The qualitative trend of $\theta$ versus $\Delta$ suggests a power-law dependence at smaller values of $\Delta$, but much slower decay at higher values. According to Zabusky *et al.* [2], thermal fluctuations become significant at higher values of $\Delta$ (and lower $\theta$), causing the slower decay similar to what was observed in Ref. [22] in MPC simulations that implicitly included thermal noise. However, the present results which do not include thermal noise tend to suggest that the thermal noise is not the only factor that is responsible for the slower decay of $\theta$. As a matter of fact, it can be said from Fig. 3 that the decay rate observed in our results is slower than that observed in the experiments, despite an increasingly large scatter in the experimental data at higher $\Delta$.

We now study the effect of capillary number $\chi$ on the numerical results. For this, we consider three values of $\chi = 1$, 10, and 50. The $\theta$ versus $\Delta$ curves are plotted in Fig. 4 for $\lambda = 1, 2.7, 5$, and 8, each for $\chi = 1, 10$, and 50. Two important observations are made here. First, for $\lambda = 1$ and 2.7, the inclination angle is nearly independent of $\chi$; only a weak dependence on $\chi$ is observed for low values of $\Delta$. This result is in agreement with that of Kraus *et al.* [16], who observed almost no $\chi$ dependence for $\lambda = 1$. On the contrary, a $\chi$ dependence can be clearly seen for $\lambda = 5$ and, in particular, for $\lambda = 8$. Thus the $\chi$ dependence appears in the numerical results as $\lambda$ increases. The same trend can be observed in the work by Zhao & Shaqfeh [23], where the $\chi$ dependence of inclination angle becomes more significant upon increasing $\lambda$. We have included two data points from their work for comparable parameters: $\lambda = 1$, $\Delta = 0.44$, $\chi = 1$ and 10, which match very well with ours. The second observation is regarding the saturation of $\theta$ at large $\chi$. As evident from the figure, the inclination angle first decreases as $\chi$ increases from 1 to 10; beyond $\chi \approx 10$, the inclination angle shows no significant change. Thus, the results for $\chi = 10$ and 50 in the figure are found to coincide. This saturation of $\theta$ at large shear rates is related to vesicle deformation. As will be shown later, the vesicle elongates more with increasing $\chi$ for up to $\chi \approx 10$. Hence, the inclination angle increases as a more elongated shape seeks to align with the flow direction. We find that the vesicle deformation saturates beyond $\chi \approx 10$, and so does the angle.

As mentioned in Sec. I, all theoretical models except Misbah's [5] predict an explicit dependence of the inclination angle on the capillary number $\chi$. Therefore, we now compare the numerical results with the theoretical models as done in Fig. 5(a). We consider the higher order models of Danker *et al.* [6] (hereafter, referred to as DBPVM), Kaoui, Farutin, & Misbah [7] (hereafter, referred to as KFM), Lebedev, Turitsyn, & Vergeles [4,13] (hereafter, referred to as LTV), and the leading order model of Misbah [5]. In the DBPVM model, the vesicle dynamics is expressed in terms of the inclination angle $\theta$ and a variable $\Theta$ associated with the vesicle shape defined as $\mathcal{R} = \sqrt{\Delta}\cos\Theta/2$, where $\mathcal{R}$ is the amplitude of deformation. Then,

$$\tau\frac{\partial\theta}{\partial t} = \frac{S}{2}\left[\frac{\cos 2\theta}{\cos\Theta}(1+\sqrt{\Delta}\Lambda_2\sin\Theta) - \Lambda\right], \tag{21}$$

$$\begin{aligned}\tau\frac{\partial\Theta}{\partial t} &= -S\sin\Theta\,\sin 2\theta + \cos 3\Theta \\ &\quad + \sqrt{\Delta}\Lambda_1 S(\cos 4\Theta + \cos 2\Theta)\sin 2\theta \\ &\quad + \sqrt{\Delta}\Lambda_2 S\cos 2\Theta\,\sin 2\theta,\end{aligned} \tag{22}$$

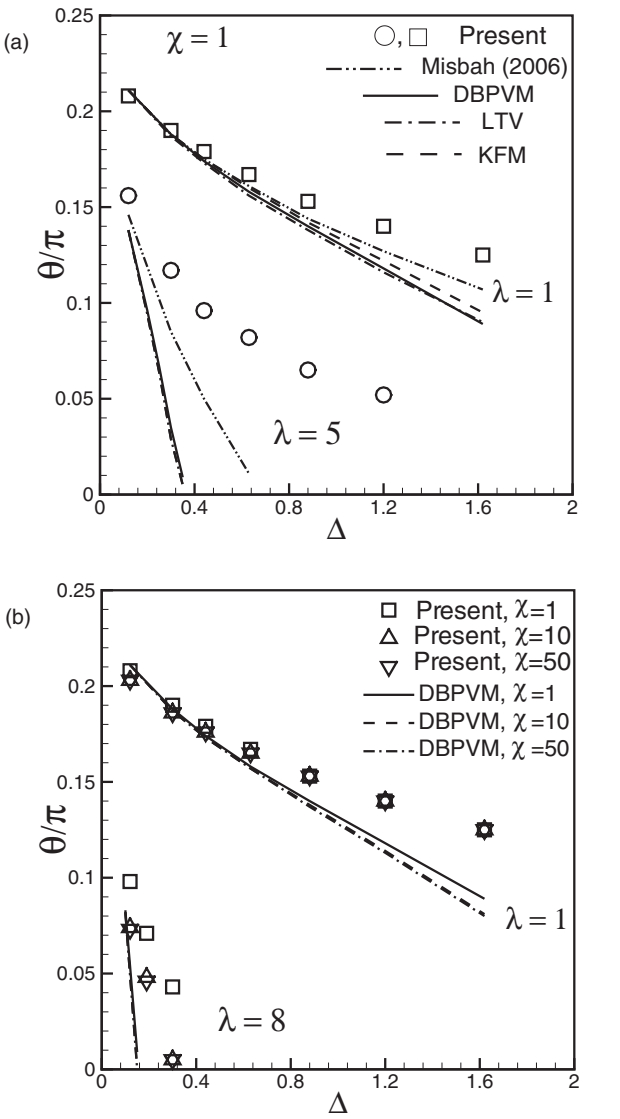


FIG. 5. (a) Comparison of the present numerical results ($\theta$ vs $\Delta$ plots) with the theoretical models for a constant $\chi = 1$, but two values of $\lambda = 1$ and 5. Theoretical models of Misbah [5], Danker *et al.* [6] DBPVM, Lebedev *et al.* [4,13] LTV, and Kaoui *et al.* [7] KFM are considered. (b) Comparison by varying $\chi$ as 1, 10, and 50, for two values of $\lambda = 1$ and 8. Here only the DBPVM model is compared to avoid cluttering of the data.

where

$$\tau = \frac{7\sqrt{\pi}(23\lambda+32)}{72\sqrt{10}}\frac{\chi}{\dot{\gamma}}, \tag{23}$$

$$\Lambda_1 = \frac{\sqrt{10}}{28\sqrt{\pi}}\left(\frac{49\lambda+136}{23\lambda+32}\right), \tag{24}$$

and

$$\Lambda_2 = \frac{10\sqrt{10}}{7\sqrt{\pi}}\left(\frac{\lambda-2}{23\lambda+32}\right). \tag{25}$$

The terms involving $\Lambda_1$ and $\Lambda_2$ are the higher order terms. From the DBPVM model, one can obtain the KFM model by setting $\Lambda_2 = 0$, the LTV model by setting $\Lambda_1 = \Lambda_2 = 0$, and Misbah's [5] model by setting $\Lambda_1 = \Lambda_2 = 0$, and omitting

the $\cos 3\Theta$ term. We solve the above system of ODEs for a tank-treading vesicle for which the inclination angle and the shape are fixed so that the left-hand sides of (21) and (22) are zero. A close form solution exists for Misbah's [5] model as $\theta = (1/2)\cos^{-1}[(23\lambda + 32)\sqrt{15\Delta}/120\sqrt{2\pi}]$. These theoretical results and the linearized form of Misbah's [5] model, $\theta = \pi/4 - (23\lambda + 32)\sqrt{15\Delta}/240\sqrt{2\pi}$, are shown in Fig. 5(a) and compared with the present front-tracking simulations. To avoid cluttering of the data, we consider $\chi = 1$ and $\lambda = 1$ and 5. The figure shows that the difference between the DBPVM, LTV, and KFM model is not significant but they differ from Misbah's model.

When we compare our numerical results with the above theoretical models [Fig. 5(a)], we find an agreement at small $\Delta$ but not at higher $\Delta$, as expected, since these models are applicable to vesicles of nearly spherical initial shapes ($\Delta \ll 1$). Interestingly, Misbah's [5] leading-order model predicts better the numerical results than the other three models. The differences between the simulation results and the theoretical results are found to increase quite significantly with increasing $\lambda$. Further, the numerical results predict a much slower decay of $\theta$ than the theoretical models, particularly for $\lambda \geqslant 5$. Hence, the theoretical models deviate from the numerical results not only at large values of $\Delta$, but also at large values of $\lambda$. Therefore, while we find that the inclination angle (weakly) depends on the shear rate as in the theoretical models, the exact nature of the dependence differs.

Figure 5(b) compares the $\chi$ dependency in theoretical models and simulations. We consider only the DBPVM model and plot the results from this model for $\chi = 1$, 10, and 50, and compare with the numerical results. There are some subtle but important differences between the two results. For $\lambda = 1$, the theoretical curves for different $\chi$ nearly collapse at lower $\Delta$ but diverge at higher $\Delta$. In contrast, the numerical results predict the opposite trend. This discrepancy might be in part due to the fact that the theoretical models are valid for small $\Delta$. Second, for higher $\lambda$, the theoretical curves for different $\chi$ are indistinguishable but the numerical results show a strong dependence on $\chi$.

### 2. *Dependence of θ on Λ*

Zabusky *et al.* [2] found that the experimental TT angles $\theta$ for different $\Delta$ collapsed when they were plotted against $\Lambda$ despite the scatter in the data due to thermal fluctuations. This finding has motivated us to present our numerical results for TT angles with respect to $\Lambda$ as well. Figure 6 shows the present numerical results for two different values of $\Delta = 0.12$ and 0.44 [Figs. 6(a) and 6(b), respectively], and the experimental data points for the closest $\Delta$ values obtained from Fig. 6 of Zabusky *et al.* Also, in the same figure, we show the DBPVM theoretical solution, and the solution given in Ref. [5], namely, $\theta = (1/2)\cos^{-1}\Lambda$. Note that the numerical results and the theoretical results by DBPVM both are presented for three values of $\chi = 1$, 10, and 50. It is clear from the figure that both the numerical and the experimental results agree well with each other within the error bars of the experiments (despite the lack of thermal noise; see error bars here and in Fig. 3). On the contrary, they both disagree with the theories not only for large values of $\Delta$ [e.g., for $\Delta = 0.44$ in Fig. 6(b)], but also for large values of $\Lambda$.

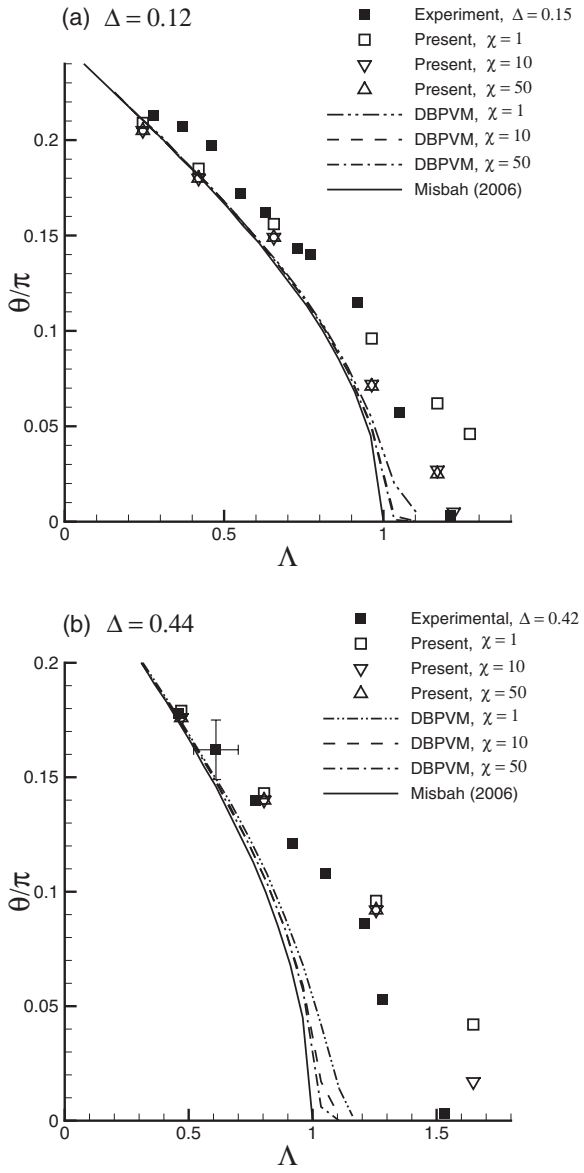


FIG. 6. Tank-treading inclination angle as a function of $\Lambda$. The numerical (open symbols) and theoretical (lines without symbols) data are plotted for different values of $\chi$; the experimental (filled symbols) data are taken from Fig. 6 of Zabusky *et al.* [2]. (a) $\Delta = 0.12$; (b) $\Delta = 0.44$.

Further, the theoretical curves for different values of $\chi$ are almost identical for small $\Lambda$ and start to branch out as $\Lambda$ increases, where the difference between $\chi = 1$ and $\chi = 10$ is more prominent. A similar trend can also be identified for the numerical results. The numerical results for $\chi = 10$ and $\chi = 50$ are almost the same for all range of $\Lambda$, but differ from those at $\chi = 1$. Thus, a collapse of data for all $\chi$ values is found in our numerical results only for small values of $\Lambda$. For higher values of $\Lambda$, a collapse may occur for $\chi \gtrsim 10$ when vesicle deformation saturates.

Now we present $\theta$ for all the numerical data points with respect to $\Lambda$ for all $\Delta$ and $\chi$ in Fig. 7. The figure shows that

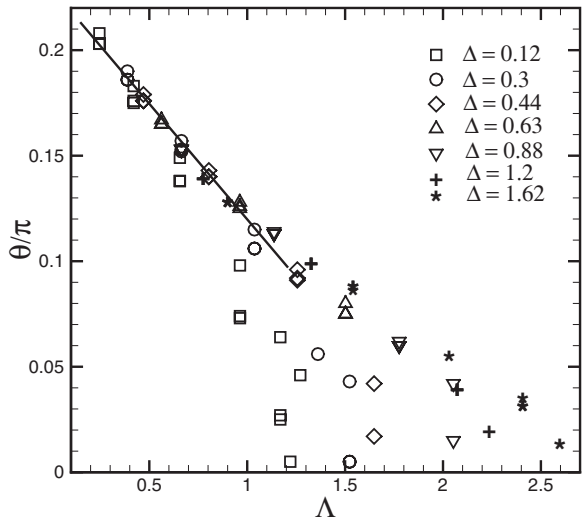


FIG. 7. Simulation results of tank-treading inclination angles $\theta/\pi$ vs $\Lambda$ plotted for all values of $\Delta$ and $\chi$ considered in the simulation. For each $\Delta$, values of $\chi$ chosen are 1, 10, and 50. A collapse is possible for approximately $\Lambda < 1$, but not for higher values.

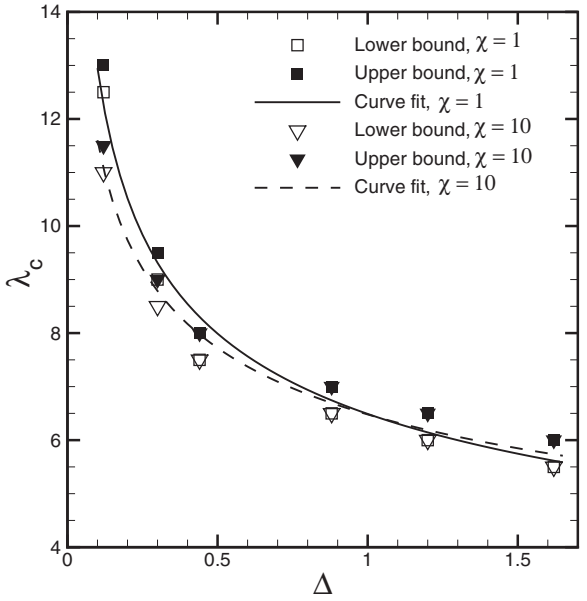


FIG. 8. Critical viscosity ratio $\lambda_c$ vs $\Delta$ obtained from the simulations. Open symbols (lower bound) correspond to the $\lambda$ values for which steady tank treading at $\theta = 0$ is observed. The filled symbols (upper bound) correspond to the $\lambda$ for which the major axis starts oscillating. Solid and dashed lines are the curve fits to the data for $\chi = 1$ and 10, respectively. The fits obey the $\lambda_c \sim \Delta^{\beta}$ relationship, where $\beta$ is $-0.3$ for $\chi = 1$, and $-0.253$ for $\chi = 10$.

the data collapse very well for approximately $\Lambda < 1$, where they can all be fitted by a straight line. The rest of data for $\Lambda > 1$, however, show a more scattered behavior and strongly vary with $\Delta$. Zabusky *et al.* noted that the quality of the experimental data did not allow one to distinguish between different sets of $\Delta$, and hence, a two-parameter scaling was sufficient within the error bars. Based on our simulation results, it is very clear that the scaling of the TT angles $\theta$ using a single variable $\Lambda$ is *only valid for small values of* $\Lambda$. The breakdown of the scaling at higher $\Lambda$ occurs even in the absence of thermal noise.

### 3. *Critical viscosity ratio*

If the data in the linear regime ($\Lambda < 1$) in Fig. 7 are fitted by a straight line, the intercept of this line with $\theta = 0$ can be taken as the critical $\Lambda_c$ for the onset of the unsteady dynamics. $\Lambda_c$, thus obtained, is a constant and independent of $\Delta$. It is informative to compare the value of $\Lambda_c$ obtained from our simulations with the theoretical and experimental values. The linear approximation of the theoretical expression of $\theta$ obtained by Misbah [5] and LTV gives $\Lambda_c = 1.57$ and 1.81, respectively. Using all $\Delta$ values (excluding the ones affected by thermal noise), Zabusky *et al.* [2] obtained $\Lambda_c = 1.74 \pm 0.2$ for the experimental data. Our simulation results yield $\Lambda_c = 1.78$ which is very close to the value found by Zabusky *et al.* and by LTV.

If one assumes that $\Lambda_c$ is a constant, then the critical viscosity ratio $\lambda_c$ varies as $\Delta^{-1/2}$. In reality, however, this scaling is not possible due to the slow (nonlinear) decay of $\theta$ as well as the breakdown of the scaling at higher $\Lambda$, as the transition is approached (see Fig. 7). Indeed, Kantsler & Steinberg [9] found that $\lambda_c \sim \Delta^{-0.24\pm0.02}$ based on their experiments. We have examined the dependence of $\lambda_c$ on $\Delta$ based on the numerical results and plotted them in Fig. 8. In order to estimate the exponent, without extrapolating the linear fit up to $\theta = 0$, we conducted simulations to clearly find when the TT angle falls to zero. The critical viscosity ratio thus obtained are presented in Fig. 8 for $\chi = 1$ and 10. We have verified that the transition threshold for $\chi = 50$ is the same as that of $\chi = 10$; hence, the $\chi = 50$ results are not shown. For each value of $\Delta$, simulations are performed in small increments of $\lambda$, until the vesicle is observed to align at $\theta = 0$ while undergoing a steady tank treading. The corresponding value of $\lambda$ is considered as the lower bound of $\lambda_c$. If $\lambda$ is further increased, the vesicle shows an oscillatory dynamics with periodic shape deformation. The onset of the oscillatory motion is taken to be the upper bound. These two bounds are plotted in the figure for $\chi = 1$ and 10. Remarkably, for approximately $\Delta > 0.5$, the results for two different $\chi$ values coincide with each other. Next, we find the curve fits through the data for $\chi = 1$ and 10. The fits obey the $\lambda_c \sim \Delta^{\beta}$ relationship as found by Kantsler & Steinberg [9]. We find the exponent $\beta$ to be $-0.3$ for $\chi = 1$, and $-0.253$ for $\chi = 10$. Hence, the exponent obtained for $\chi = 10$ is in excellent agreement with the experimentally derived exponent of $-0.24 \pm 0.02$ by Kantsler & Steinberg [9]. This agreement is remarkable despite the absence of thermal noise in our simulations. The exponent for $\chi = 1$ data found here is slightly lower than the experimental value, since the experiments were performed mostly for $\chi > 1$. It should be mentioned that the method used to find $\lambda_c$ is different than those used in previous studies, e.g., in Zhao & Shaqfeh [23], where $\lambda_c$ was calculated through linear stability analysis of the steady-state solution. In that analysis a steady-state tank-treading motion with negative inclination angles can be achieved for $\lambda$ values close but less than $\lambda_c$, which are not observed here. Further, most theoretical

studies, e.g., Farutin *et al.* [14], and the analysis of Zhao & Shaqfeh [23] show that $\lambda_c$ increases with $\chi$. Since here we find $\lambda_c$ by considering actual simulations in finite steps of increasing $\lambda$, it is difficult to conclude from the figure how $\lambda_c$ depends on $\chi$.

#### 4. Deformation

The deformation of the tank-treading vesicles is quantified by the Taylor deformation parameter $D = (L - B)/(L + B)$, where $L$ and $B$ are the semimajor and minor axes of the ellipsoidal contour in the shear plane. Figure 9(a) shows $D$ versus $\chi$ for different values of $\Delta$, but for a fixed $\lambda = 1$. The results show that deformation first increases with increasing $\chi$, suggesting a nonlinear behavior in the range $1 \lesssim \chi \lesssim 10$. Upon further increase in $\chi$, deformation is found to saturate. This result is qualitatively similar to the experimental findings of Kantsler & Steinberg [18] and the theoretical prediction of Seifert [11] that $D$ is independent of $\chi$ for large values.

It may be noted that the thermal effect is usually dominant at small $\chi$ as is the case in Seifert's [11] model and in Kantsler & Steinberg's [18] experiments. Seifert [11] predicted that $D$ increases linearly with $\chi$ for vanishingly small values of $\chi$, and shows nonlinear behavior at the crossover followed by a saturation for sufficiently large values of $\chi$. Kantsler & Steinberg [18] also observed a nonlinear behavior of $D$ for small values of $\chi$. It is quite remarkable that a nonlinear behavior of $D$ is possible in the range $\chi \lesssim 10$, even in the absence of thermal noise, as found in our simulations.

Quantitative comparison with Seifert's [11] prediction, Kantsler & Steinberg's [18], and the Kantsler *et al.* [39] experimental results is given in Fig. 9(a) by plotting $D$ versus $\sqrt{\Delta}$. In this figure, we show all of our data points over the range of $\lambda$ considered in the simulations, and for $\chi = 1$ and 10. For clarity, $\chi = 50$ data are not shown as they coincide with those of $\chi = 10$. In the limit of large $\chi$, Seifert predicted

$$D = \sqrt{15\Delta/32\pi}\,. \tag{26}$$

In addition to the nearly spherical limit, Seifert's analysis is also limited to "weak" external flow. Despite these limitations, the theoretical line seems to match surprisingly well with the simulation results in the approximate range of $\Delta < 1$. For $\Delta > 1$, the theory overpredicts the simulation results.

The experimental data points shown in Fig. 9(b) are taken from two sources: from Fig. 5 of Kantsler & Steinberg [18] for the highest values of $\chi E_b/k_BT$ given therein, where $k_B$ is the Boltzmann constant and $T$ is the room temperature, and from Fig. 1 of Kantsler *et al.* [39] by averaging $D$ after it reached a steady state with respect to time. Keeping in mind the uncertainty in the experimental data, a good agreement with our simulation results is also evident.

Two interesting observations are worth mentioning. First, the saturation of $D$ occurs at $\chi \approx 10$ which holds for all values of $\Delta$ and $\lambda$. Second, the trend of $D$ with increasing $\chi$ can explain the dependence of $\theta$ on $\chi$ as noted earlier in Fig. 4. For $\chi = 1$ to 10, $D$ increases, and hence, $\theta$ decreases as more elongated objects tend to align with the flow direction. Beyond $\chi \approx 10$, deformation saturates, and so does inclination.

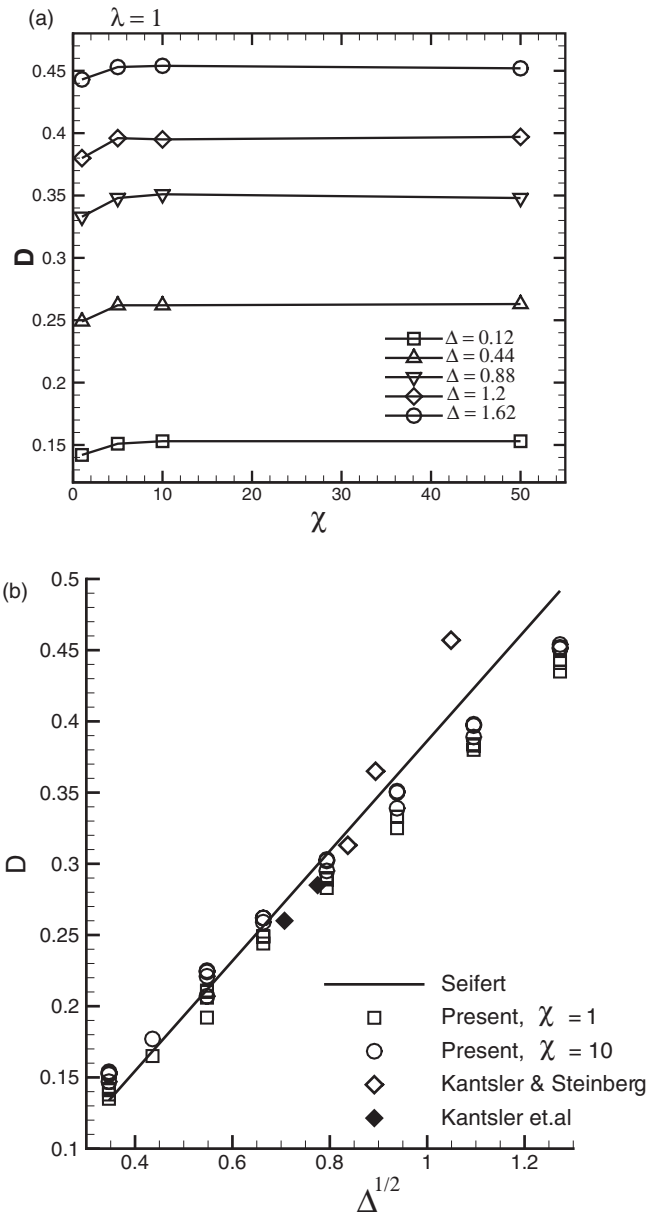


FIG. 9. (a) Taylor deformation parameter $D$ vs capillary number $\chi$ for $\lambda = 1$, and different values of $\Delta$. (b) $D$ vs $\sqrt{\Delta}$ for all $\lambda$ considered in the simulations, and for $\chi = 1$ and 10. For clarity, $\chi = 50$ data are not shown as they coincide with those of $\chi = 10$. Also shown in (b) are the theoretical prediction by Seifert [11] and experimental data of Kantsler & Steinberg [18] and Kantsler *et al.* [39]. The experimental data points are taken from Fig. 5 of Kantsler & Steinberg for large $\chi$ values (the data points for the highest values of $\chi E_b/k_BT$ given in that paper), and from Fig. 1 of Kantsler *et al.* (averages of $D$ are taken after $D$ reached a steady state with respect to time given therein).

### B. Transition and tumbling modes

#### 1. Analysis of vesicle shapes

We now turn attention to the unsteady regimes of vesicle dynamics. In general, two types of unsteady dynamics are observed. First is the usual tumbling motion resembling a rigid-body flipping. The second dynamics which is more difficult

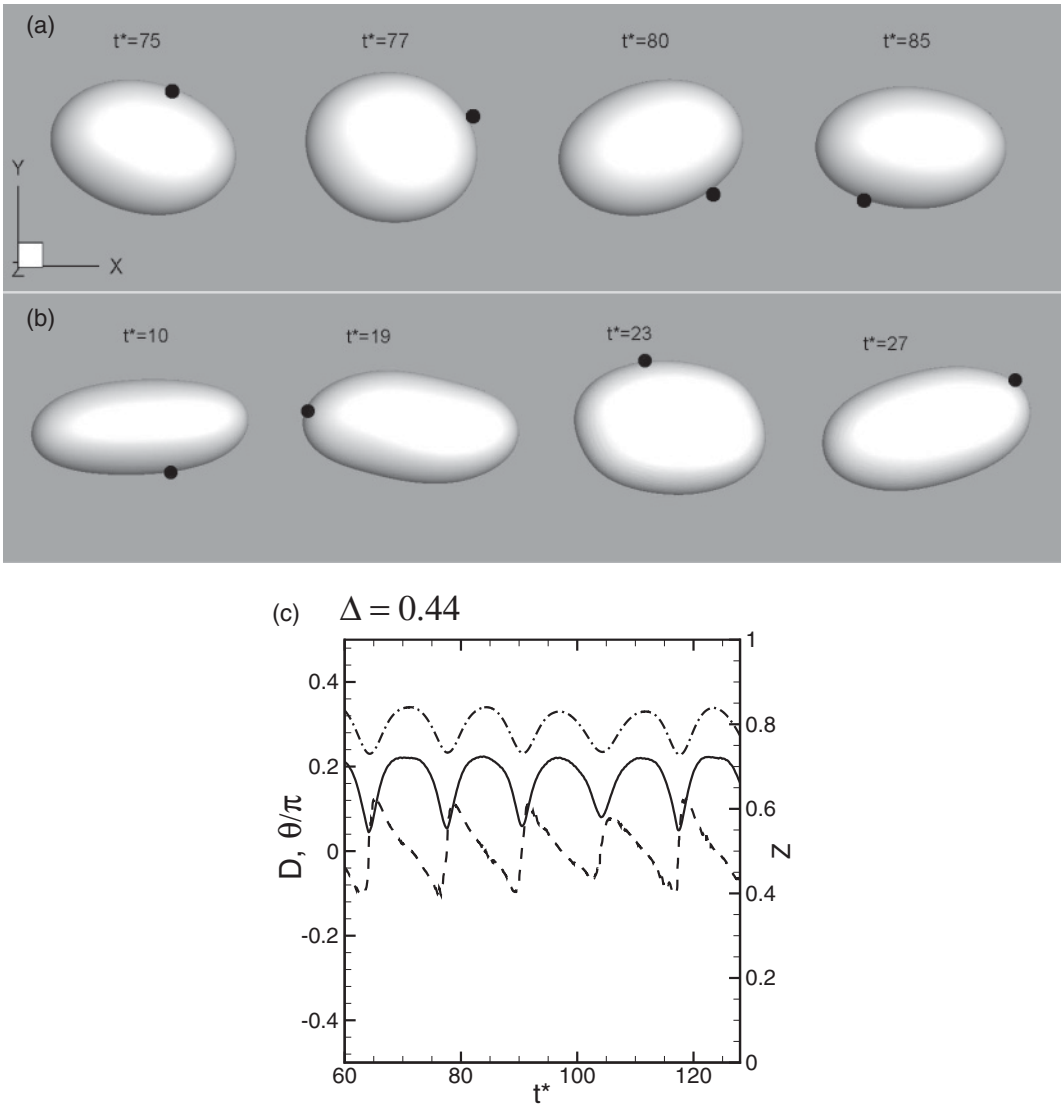


FIG. 10. Simulation results on the vacillating-breathing-like dynamics similar to that predicted by the theories: (a) $\Delta = 0.44$, $\lambda = 10$, $\chi = 5$; (b) $\Delta = 1.2$, $\lambda = 7$, $\chi = 10$. A Lagrangian marker point is tracked in the snapshots which shows that the membrane executes a TT motion. (c) Time-dependent deformation parameter $D$ (left axis, solid line), inclination angle $\theta$ (left axis, dashed line), and the half of end-to-end length $Z$ in the vorticity direction (right axis, dash-dotted line) for the case shown in (a).

to analyze is the one that occurs on the verge of transition between the TT and TU motion. Depending on the details of the dynamics, this mode has been identified by various names, e.g., vacillating breathing (Misbah & co-workers), trembling (Steinberg & co-workers), and swinging (Noguchi & Gompper). Specifically, the vacillating-breathing mode predicted in the theoretical work is characterized by smooth elliptical contours undergoing time-dependent shape oscillation and angular oscillation about $\theta = 0$. In contrast, the trembling mode observed in the experiments is characterized by highly convoluted vesicle shapes. In the present work, both modes are grouped as the "transition" mode. As will be shown below, our simulations predict that both the vacillating-breathing-like motion and the trembling-like motion are possible in the transition zone.

Figure 10 shows two sample results for the *vacillating-breathing*-like motion. As evident, the vesicle shape remains nearly elliptical with time while it undergoes angular oscillation about $\theta \approx 0$. A significant shape oscillation accompanies the angular oscillation resembling a breathing-like dynamics. For $\Delta = 0.44$ shown in Fig. 10(a), the shapes look qualitatively similar to the contours given in Ref. [6]. Higher order even harmonics are particularly evident in Fig. 10(b) where $\Delta = 1.2$ is considered. The time-dependent inclination angle $\theta$, deformation parameter $D$, and the half of the end-to-end length $Z$ in the vorticity direction are plotted in Fig. 10(c). Large oscillation in $D$ is observed. Further, $Z$ versus time shows that shape oscillation in the out-of-the-flow-plane direction could be significant as noted by Vlahovska & Gracia [12] in their theoretical work.

The vacillating-breathing-like motion described above occurs in our simulations for low values of $\chi$, and in the vicinity of $\lambda_c$ which corresponds to the border between the tank-treading and transition zone (see Fig. 16 below). For

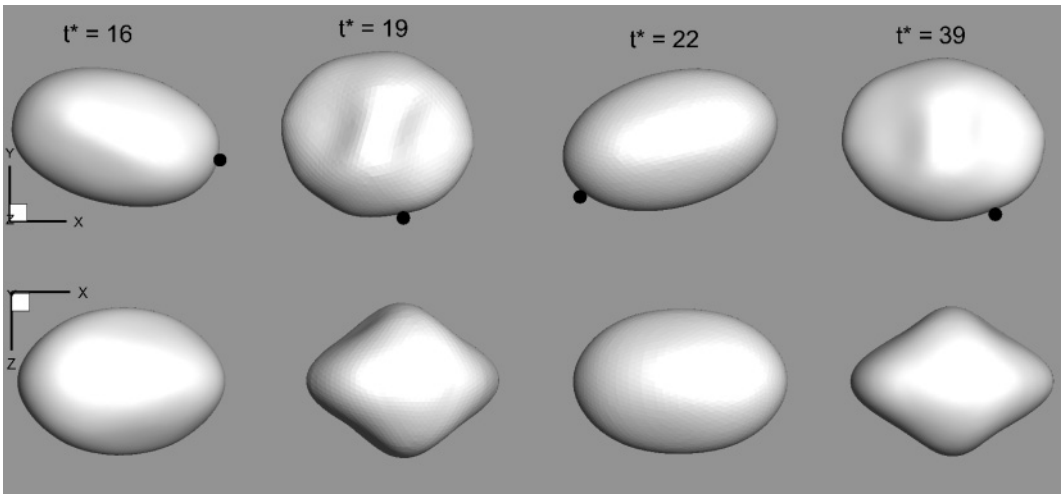


FIG. 11. Simulation results of a vesicle in the transition region resembling a trembling-like motion. Here $\Delta = 0.44, \lambda = 8, \chi = 50$. Top row shows the view in the shear plane ($x$-$y$ plane), and the bottom row shows the view along the velocity gradient ($x$-$z$ plane). Fourth-order harmonics are present in $x$-$z$ contours when the vesicle is aligned in the compressional quadrant ($t^* = 19$ and 39, above). A Lagrangian marker point on the vesicle surface suggests that the membrane makes an oscillatory tank-treading motion.

higher values of $\chi$ and $\lambda$ (near the border between the transition zone and tumbling zone), vesicles show convoluted deformed shapes resembling the *trembling*-like behavior. One such result is shown in Fig. 11. Remarkably, the vesicle assumes a diamond shape in the $x$-$z$ plane (view along the velocity gradient direction) periodically when its long axis drops below $\theta = 0$ ($t^* = 19$ and 39 in the figure). The smooth elliptical shape is recovered when the vesicle is aligned above $\theta = 0$. We have performed Fourier transform of the contours of the vesicle in $x$-$y$ and $x$-$z$ planes (see below for more details), and found that the fourth harmonics is comparable to the second for the $x$-$z$ contour when the vesicle is in the compressional quadrant of the flow. In contrast, for the $x$-$y$ contour, the higher order harmonics are much weaker compared to the second harmonics. Clearly, the vesicle exhibits more deformation and more harmonics along the vorticity direction than on the shear plane. This result underscores the importance of three-dimensional effects for the vesicles in the transition region.

Another sample result for the *trembling*-like dynamics is shown in Fig. 12 corresponding to $\Delta = 1.2$, $\lambda = 7.5$, and $\chi = 50$. The vesicle becomes highly deformed with concavities and lobes when it is aligned in the compressional quadrant ($t^* = 21$ in the figure). The convoluted shape observed here is qualitatively similar to the experimentally observed shapes (Zabusky *et al*. [2]). The shape is highly three-dimensional with more deformation occurring along the vorticity direction. Figure 12(b) shows the contour of the vesicle in the $x$-$z$ plane to further emphasize the appearance of concave regions on the vesicle surface. The contour also shows an asymmetry along the $z$ direction implying the presence of the *odd* harmonics.

It is worth mentioning that in our simulations the higher modes are observed mostly when the vesicle is in the compressional quadrant. These instabilities are suppressed when the vesicle aligns in the extensional quadrant, and the smooth elliptical shape is recovered. The vesicle spends a longer time in the extensional quadrant so that the bending forces restore the shape. In the next cycle again the higher modes appear in the compressional quadrant. If the thermal noise were present, these modes would have sustained in the extensional quadrant as well, as observed in the experiments (Zabusky *et al*. [2]). Further, no mesh skewing is observed for such complex shapes, the simulations were done with 20480 Lagrangian elements, and the volume correction is not needed. The irregular shapes observed here are only for the vesicles that are near the transition borderline. For the vesicles that are far away from the transition border, such irregularities are not observed.

Figure 13 shows the Fourier spectra of the vesicle contours shown in Fig. 12 for three time instants when the vesicle is within and near the compressional quadrant. We consider the radial amplitude of the contour $R(\phi,t), 0 \leqslant \phi \leqslant 2\pi$, relative to the centroid of the vesicle [2], which is Fourier decomposed as $R(\phi,t) = \sum_k \tilde{R}_k(t) e^{ik\phi}$. Higher order even modes beyond the fourth harmonics are observed for both $x$-$y$ and $x$-$z$ contours. Odd modes appear in the $x$-$z$ contour at $\theta/\pi = -0.18$, when the vesicle is near the compressional axis. It should be mentioned that the odd harmonics are generated here by numerical noise.

The convoluted shapes can also appear during the tumbling motion at higher values of $\chi$. One such example is shown in Fig. 14(a) for $\Delta = 0.44$, $\lambda = 12$, and $\chi = 50$. Concavity in the vesicle shape is observed here when it is aligned in the compressional quadrant. Of course, the amount of deformation is much less than that observed earlier for the trembling-like motion. The concavities disappear and the smooth elliptical shape is recovered as the vesicle enters the extensional quadrant. Another example is shown in Fig. 14(b) at lower values of $\chi = 1$ to illustrate the effect of shear rate on vesicle deformation in the tumbling regime. For this low value of $\chi$ the vesicle deformation from its equilibrium is almost negligible, and no membrane concavity is observed.

### 2. *Transient dynamics*

Within the transition region, we find that the dynamics is often transient in nature; in other words, the vesicle starts

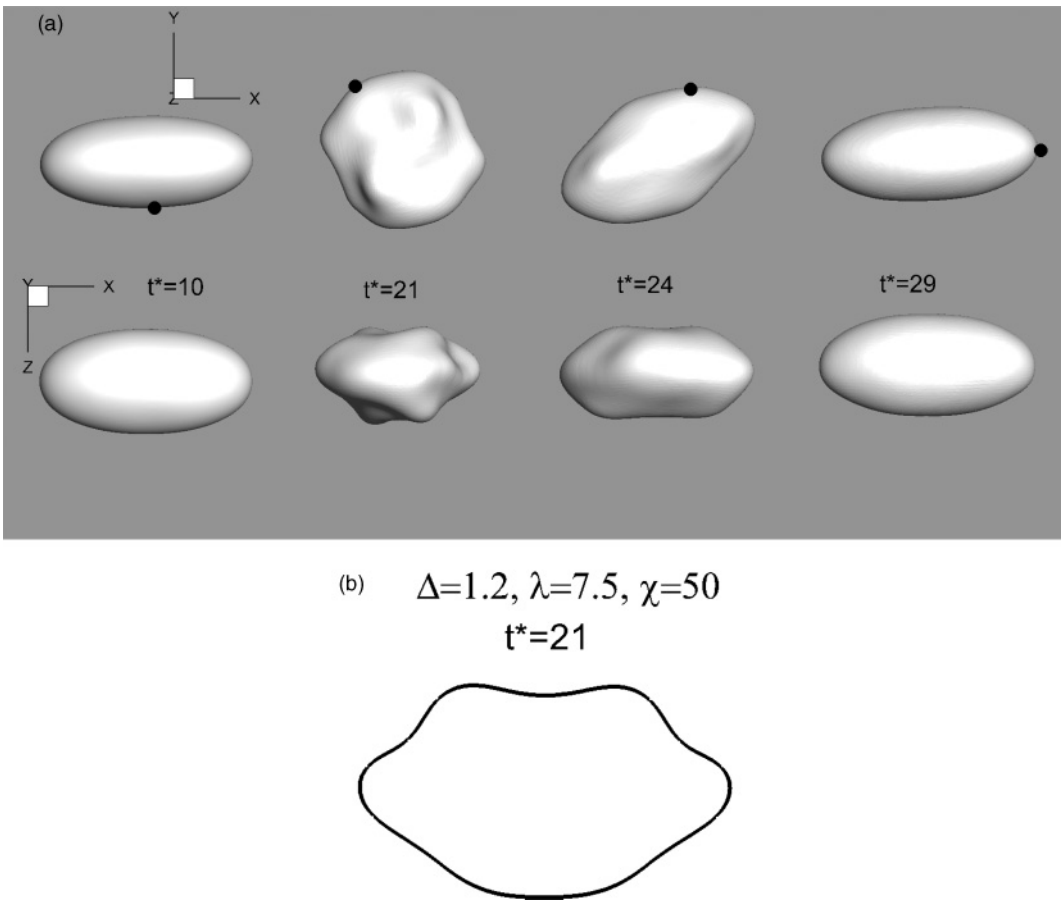


FIG. 12. (a) Simulation results of a vesicle near the border of transition/tumbling zone resembling a trembling-like motion with highly deformed shape. Here $\Delta = 1.2, \lambda = 7.5, \chi = 50$. Top row shows the view in the shear plane ($x$-$y$ plane), and the bottom row shows the view along the velocity gradient ($x$-$z$ plane). A Lagrangian marker point shows that the membrane makes a net tank-treading motion. (b) Vesicle contour is shown in the $x$-$z$ plane at $t^* = 21$.

with one mode, and then settles to another after a long time. Typically, we find two types of transient dynamics: In the first case, which occurs at the border between the tank-treading and the transition zones, the vesicle starts with a swinging

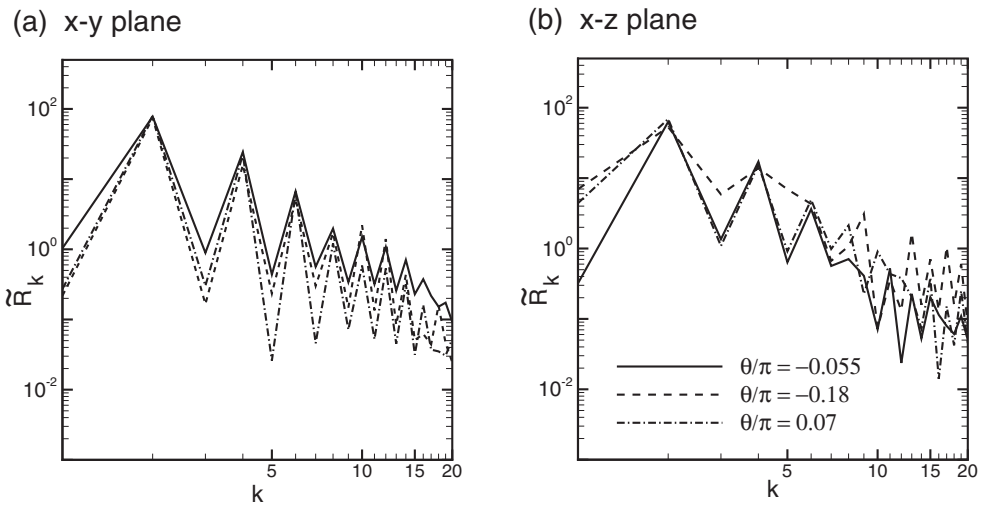


FIG. 13. Fourier spectra of vesicle contours for $\Delta = 1.2, \lambda = 7.5, \chi = 50$ showing higher modes for three different inclination angles within or near the compressional quadrant. (a) Spectra for $x$-$y$ contours, and (b) $x$-$z$ contours. The modes higher than fourth-order and odd modes in the $x$-$z$ contours are observed.

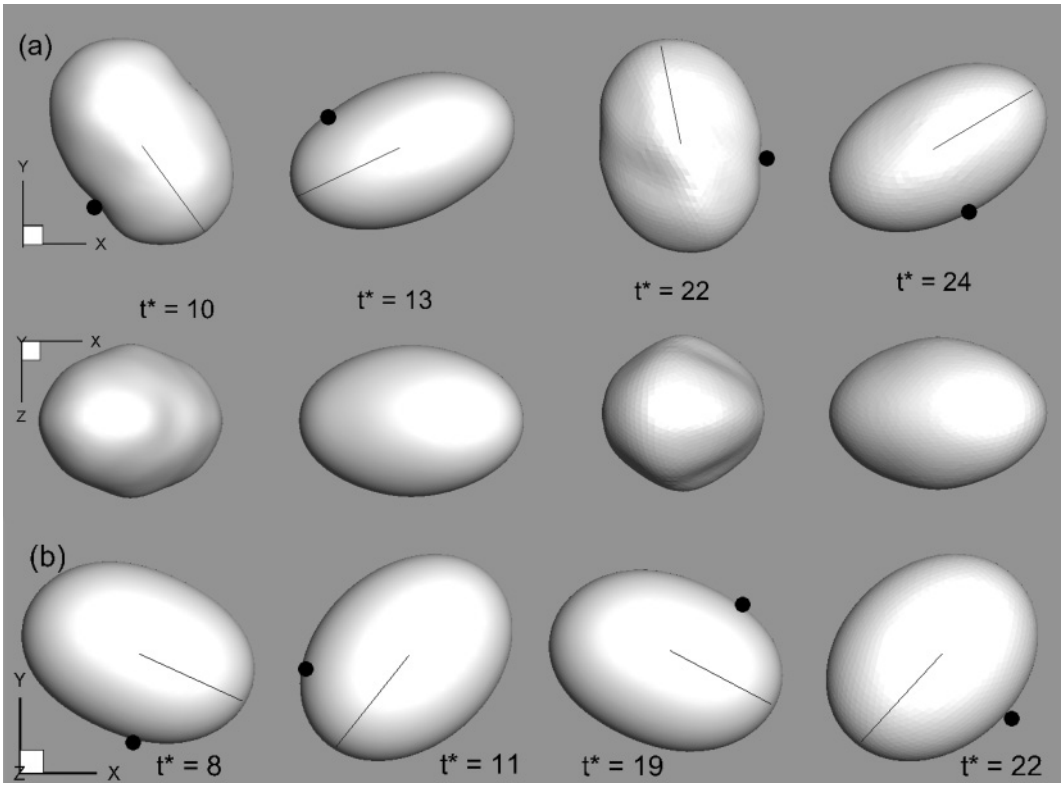


FIG. 14. Snapshots of tumbling vesicles: (a) $\Delta = 0.44, \lambda = 12, \chi = 50$ which shows that concavity can appear in the tumbling motion at higher $\chi$ values. Here both views in the shear plane ($x$-$y$) and along the velocity gradient direction ($x$-$z$ plane) are shown. (b) $\Delta = 0.44, \lambda = 12, \chi = 1$ which shows a smooth elliptical shape at lower $\chi$ values. Only the shear plane view is shown here.

motion and settles to a tank-treading motion; in the second type, it starts with a tumbling motion and gradually relaxes to a swinging motion. The first situation is presented in Fig. 15(a) for $\lambda = 8$ and $\chi = 10$. For this case the vesicle initially shows oscillatory deformation and swinging motion, but the amplitudes of oscillation and deformation slowly decrease over time. Eventually the vesicle aligns with the flow direction after about three oscillations. This form of transient dynamics toward tank-treading motion is similar to the relaxation dynamics of a vesicle close to the border between the tank-treading and transition zone observed by Biben *et al*. [15]. Zhao & Shaqfeh [23] have also shown that the decay of the most unstable mode of the stable tank-treading solution is the source of this behavior. The second type of the transient dynamics occurs upon increasing $\lambda$, and is shown in Fig. 15(b) for $\lambda = 10$ and $\chi = 5$. Here the vesicle tumbles initially, and then gradually relaxes to the final swinging dynamics at around $t^* \approx 80$. We also studied the effect of the shear rate on the transient dynamics by keeping the same viscosity ratio, and found that higher shear rates will delay the relaxation to the final mode by several more cycles. Note that higher shear rates will reduce the flow time scale, which in turn will prolong the relaxation.

### 3. *Phase diagram*

The phase diagrams from our numerical simulations for two values of $\Delta = 0.44$ and 1.2 in the $\chi$-$\lambda$ plane are presented in Figs. 16(a) and 16(b), respectively. Based on the dynamics described above, three regions are identified in the phase diagrams: (i) tank treading, (ii) transition, and (iii) tumbling. The general nature of the diagrams is similar to that predicted by the experiments and the theoretical models: For small values of $\chi$, the transition occurs directly as TT $\rightarrow$ TU with increasing $\lambda$, and for $\chi \gtrsim 1$, the vacillating-breathing or the trembling modes appear. We find that the vacillating-breathing mode appears near the lower bound of the transition region, and the trembling-like dynamics occurs near the upper bound. The lower and the upper bounds are independent of $\chi$ for large values. The qualitative nature of the phase diagrams is similar for $\Delta = 0.44$ and 1.2, except that the transition boundaries shifted downward for the latter.

Certain differences exist in comparison to the experiments and the theoretical models. First, the width of the transition zone obtained from our simulations is higher than that predicted by the theoretical models of KFM, DBPVM, and LTV. From our phase diagram for $\Delta = 0.44$, the range of $\lambda$ for the transition zone appears to be 7.5 to 10, corresponding to the lower and upper bounds, respectively. On the contrary, the KFM model predicts 5.92 to 6.7, the DBPVM modes predicts 5.97 to 6.65, and the LTV model predicts 5.87 to 6.33 (see Table I in Zabusky *et al*. [2]), giving a much narrower transition band even for such a relatively low value of $\Delta$. It should be noted that in the figure, the bold lines are for visual guide only, as one would need more simulations to improve the prediction of the transition borders. Moreover, in the transition zone marked as (ii) in the figure, there are two types of the transient dynamics: In one the vesicle relaxes from a swinging to a tank-treading motion, and in another it

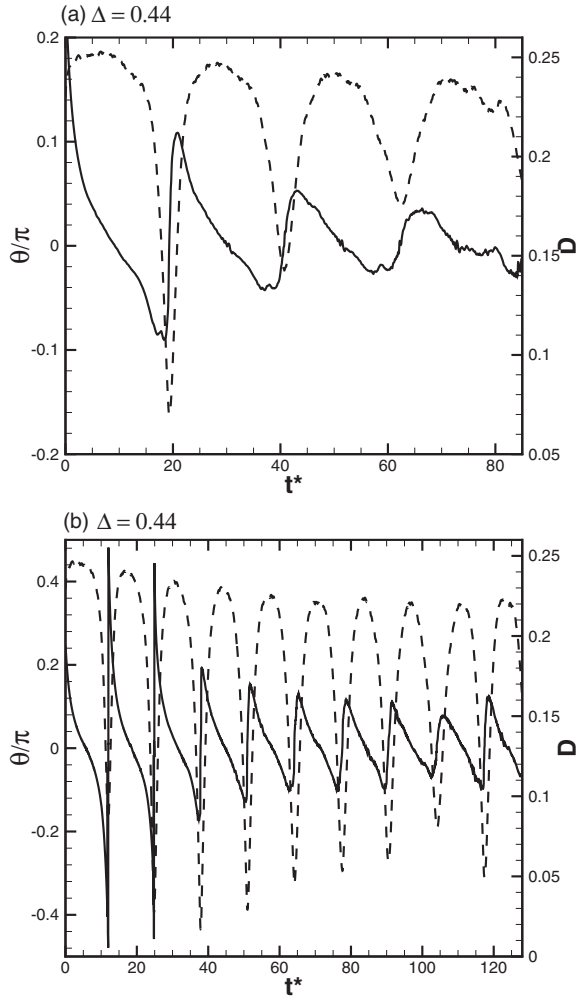


FIG. 15. Transient dynamics observed for vesicles in the transition zone. Time evolution of $\theta$ and $D$ are shown. (a) $\Delta = 0.44$, $\lambda = 8, \chi = 10$. Here the dynamics changes from swinging to tank treading. (b) $\Delta = 0.44$, $\lambda = 10, \chi = 5$. Here the dynamics changes from tumbling to swinging.

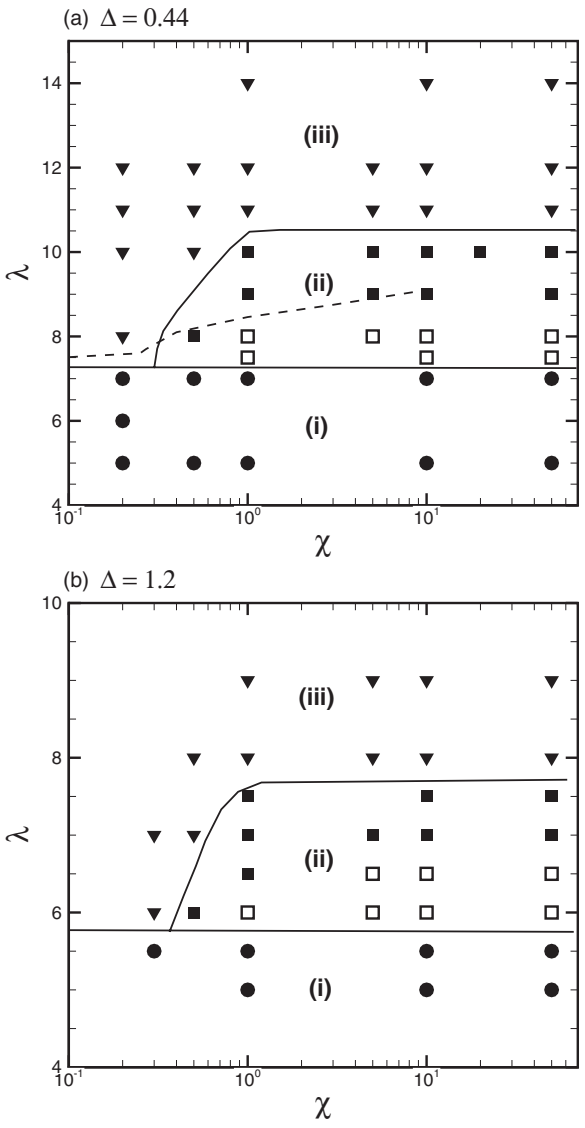


FIG. 16. Phase diagram for the vesicle dynamics in linear shear flow for (a) $\Delta = 0.44$, (b) $\Delta = 1.2$. (i) Tank-treading zone (filled circles). (ii) Transition zone: (filled squares) initially tumbling motion relaxes to swinging dynamics, and (open squares) initially swinging dynamics relaxes to tank-treading motion along the flow direction. (iii) Tumbling zone (filled triangles). Also shown in (a) the stability boundary between tank-treading and tumbling/transition dynamics evaluated by Zhao & Shaqfeh [23] from the linear stability analysis (dashed line). Bold lines are a guide for the eyes.

relaxes from a tumbling to swinging motion. We identify these two types of transient motion in the figure. We also include the neutral curve calculated by Zhao & Shaqfeh [23] for $\Delta = 0.44$. The swinging-to-tank-treading region falls below the stability boundary, and hence, there is an overall agreement between the two works.

Second, the phase diagrams reported in the experiments by Deschamps *et al*. [3] and Zabusky *et al*. [2] are plotted in the $S$-$\Lambda$ plane. The range of the trembling band from their phase diagram is $\Lambda \sim 1.5$ to 2.25. Note that these two bounds appear to be independent of $\Delta$ values within the margin of uncertainty in the experimental data suggesting a self-similar behavior in the two-parameter space. When we try to scale our data in the two-parameter space, we find that the results are not independent of $\Delta$. In other words, the lower and upper bounds of $\Lambda$ are functions of $\Delta$. Specifically, we find that the lower and upper bounds are $\Lambda \approx 1.75$ and 2.24 for $\Delta = 0.44$, and 2.4 and 2.88 for $\Delta = 1.2$. Thus, the transition band shifts upward with increasing $\Delta$. Hence, we do not find the self-similar behavior in the two-parameter space, unlike found by the LTV model and in the experimental analysis of Zabusky *et al*. [2]. However, Zabusky *et al*.'s plot appears to suggest a transition band of ~0.75, which is higher than our value. This discrepancy could arise due to the presence of the thermal noise in the experiments, as well as the experimental uncertainty.

Third, Farutin *et al*. [14] in their recent analytical work and Biben *et al*. [15] in their recent boundary integral simulations have shown that the inclusion of the fourth-order harmonics in vesicle shape widens the transition band upon increasing $\chi$. Their analytical and numerical predictions for the transition band are close to our results. On the contrary, the transition band found in our simulations does not show such widening effect for the range of $\chi$ up to 50 considered. Further, similar

to the KFM model, we observe that the transition band in the $\chi$-$\lambda$ plane becomes narrower as $\Delta$ increases.

## IV. CONCLUSION

We presented a 3D numerical simulation of vesicle dynamics in shear flow using the front-tracking method. Our numerical technique is able to simulate the vesicles in the tank-treading, vacillating-breathing, trembling, and tumbling modes. The main objectives were to elucidate the parametric dependence and the self-similarity of the vesicle dynamics, quantification of vesicle deformation, and the analysis of shape dynamics in the trembling mode. The front-tracking method presented here is an alternative to the boundary integral method, which has been often used for the vesicle simulations. The choice of the front-tracking method over the boundary-integral method is due to the straightforward implementation and versatility. The current method can be readily extended to include membrane shear resistance (e.g., [35]), membrane viscosity, and most importantly finite Reynolds number effect, which could be the case for giant vesicles. Further, the present method is very stable over a large range of the control parameters, such as shear rate, viscosity contrast, bending stiffness, etc., and hence long simulations can be performed without losing numerical stability. In contrast, in the boundary integral method by Kraus *et al*. [16], the effect of $\lambda$ is not considered. In addition, in case of a structured grid of the vesicle surface, there is the possibility of mesh entanglement in the poles which is not the case here. We do not observe local coarsening or entanglement of surface mesh over the length of the simulations; thus, no remeshing is done. It is also encouraging that the results from our simulations agree well with the spectral accurate simulations of Zhao & Shaqfeh [23]. A comparison of the numerical efficiency of different methods, however, is beyond the scope of this work.

In general we find an agreement with the notion set forth in Zabusky *et al*. [2] that the applicability of the perturbative results is limited despite some general agreement with the direct numerical simulations and experiments. Here we find that many of the deviations between the perturbative results and the simulation results occur even in the absence of thermal noise.

The major findings of this article are as follows:

(i) We do not observe a self-similar behavior of the vesicle dynamics in the two-parameter phase space proposed by the LTV model and suggested by Zabusky *et al*. in their analysis of the experimental data. Rather, we find that the phase boundaries depend on the excess area even when plotted in the two-parameter space. In other words, the dynamics is governed by three controlling parameters, namely, $\Delta$, $\lambda$, and $\chi$, as in the models of DBPVM and KFM.

(ii) The linear scaling of the TT angle using $\Lambda$ is valid only for $\Lambda < 1$. The breakdown of the scaling at higher $\Lambda$ occurs even in the absence of thermal noise.

(iii) We show that in the transition regime, both the vacillating-breathing-like motion characterized by a smooth elliptical shape and the trembling-like motion characterized by highly deformed shape are possible. For the trembling-like motion, the shape is highly three-dimensional with concavities and lobes, and the vesicle deforms more in the vorticity direction than in the shear plane. This result underscores the importance of three-dimensionality in vesicle dynamics. A Fourier spectral analysis of the vesicle shape shows the presence of the odd harmonics and higher order modes beyond fourth order.

(iv) Our estimation of the critical viscosity ratio $\lambda_c$ is in excellent agreement with the experimental observation of $\lambda_c \sim \Delta^{0.24\pm0.02}$ by Kantsler & Steinberg [9]. The computed tank-treading angles are also in very good agreement with the experimental measurements within the margin of uncertainty. Similar to the experimental findings, the numerical TT angles deviate significantly from the theoretical results at large values of $\Delta$. Despite the absence of thermal noise in the simulations, the slow decay of the TT angles found here agreed very well with the experimental observation.

(v) Similar to the DBPVM, KFM, and LTV models, we find an explicit dependence of the tank-treading angle on $\chi$ for small values, but saturation at higher values. However, contrary to the models, $\chi$ dependence is observed to increase with increasing $\lambda$.

(vi) In agreement with Seifert's prediction [11], and experimental measurements by Kantsler & Steinberg [18], we find that vesicle deformation saturates with increasing $\chi$. Quantitatively, we find that Seifert's prediction of $D = \sqrt{15\Delta/32\pi}$ for nearly spherical vesicles at $\chi \to \infty$ agreed very well with the numerical results in the range $\Delta < 1$.

## ACKNOWLEDGMENTS

This research is funded by NSF Grant No. CBET-0846293. Computational support from the NSF-funded Teragrid resources at TACC and NCSA is acknowledged.

[1] S. R. Keller and R. Skalak, J. Fluid Mech. **120**, 27 (1982).
[2] N. J. Zabusky, E. Segre, J. Deschamps, V. Kantsler, and V. Steinberg, Phys. Fluids **23**, 041905 (2011).
[3] J. Deschamps, V. Kantsler, and V. Steinberg, Phys. Rev. Lett. **102**, 118105 (2009).
[4] V. V. Lebedev, K. S. Turitsyn, and S. S. Vergeles, Phys. Rev. Lett. **99**, 218101 (2007).
[5] C. Misbah, Phys. Rev. Lett. **96**, 028104 (2006).
[6] G. Danker, T. Biben, T. Podgorski, C. Verdier, and C. Misbah, Phys. Rev. E **76**, 041905 (2007).
[7] B. Kaoui, A. Farutin, and C. Misbah, Phys. Rev. E **80**, 061905 (2009).
[8] H. Noguchi and G. Gompper, Phys. Rev. Lett. **98**, 128103 (2007).
[9] V. Kantsler and V. Steinberg, Phys. Rev. Lett. **96**, 036001 (2006).
[10] M.-A. Mader, V. Vitkova, M. Abkarian, A. Viallat, and T. Podgorski, Eur. Phys. J. E **19**, 389 (2006).
[11] U. Seifert, Eur. Phys. J. B **8**, 405 (1999).

[12] P. M. Vlahovska and R. S. Gracia, Phys. Rev. E **75**, 016313 (2007).
[13] V. V. Lebedev, K. S. Turitsyn, and S. S. Vergeles, New J. Phys. **10**, 043044 (2008).
[14] A. Farutin, T. Biben, and C. Misbah, Phys. Rev. E **81**, 061904 (2010).
[15] T. Biben, A. Farutin, and C. Misbah, Phys. Rev. E **83**, 031921 (2011).
[16] M. Kraus, W. Wintz, U. Seifert, and R. Lipowsky, Phys. Rev. Lett. **77**, 3685 (1996).
[17] K. H. de Haas, C. Blom, D. van den Ende, M. H. G. Duits, and J. Mellema, Phys. Rev. E **56**, 7132 (1997).
[18] V. Kantsler and V. Steinberg, Phys. Rev. Lett. **95**, 258101 (2005).
[19] T. Biben, K. Kassner, and C. Misbah, Phys. Rev. E **72**, 041921 (2005).
[20] G. Ghigliotti, T. Biben, and C. Misbah, J. Fluid Mech. **653**, 489 (2010).
[21] H. Noguchi and G. Gompper, Phys. Rev. E **72**, 011901 (2005).
[22] S. Messlinger, B. Schmidt, H. Noguchi, and G. Gompper, Phys. Rev. E **80**, 011901 (2009).
[23] H. Zhao and E. S. G. Shaqfeh, J. Fluid Mech. **674**, 578 (2011).
[24] S. K. Veerapaneni, D. Gueyffier, G. Biros, and D. Zorin, J. Comput. Phys. **228**, 7233 (2009); S. K. Veerapaneni, A. Rahimian, G. Biros, and D. Zorin, *ibid*. **230**, 5610 (2011).
[25] W. Helfrich, Z. Naturforsch. C **28**, 693 (1973).
[26] O.-Y. Zhong-can and W. Helfrich, Phys. Rev. A **39**, 5280 (1989).
[27] G. Tryggvason, B. Bunner, A. Esmaeeli, N. Al Rawahi, W. Tauber, J. Han, S. Nas, and Y. Jan, J. Comput. Phys. **169**, 708 (2001).
[28] R. V. Garimella and S. Swartz, Tech. Rep. LA-UR-03-8240,2003 (unpublished).
[29] S. Petitjean, ACM Comput. Surv. **34**, 211 (2002).
[30] M. Reuter, S. Biasotti, D. Giorgi, G. Patane, and M. Spagnuolo, Comput. Graph. **33**, 381 (2009).
[31] G. Xu, Comput. Math. Appl. **48**, 347 (2004).
[32] R. Skalak, A. Tozeren, P. R. Zarda, and S. Chien, Biophys. J. **13**, 245 (1973).
[33] S. K. Doddi and P. Bagchi, Int. J. Multiphase Flow **34**, 966 (2008).
[34] S. Shrivastava and J. Tang, J. Strain Anal. **28**, 31 (1993).
[35] A. Z. K. Yazdani and P. Bagchi, Phys. Rev. E **84**, 026314 (2011).
[36] Z. Peng, R. J. Asaro, and Q. Zhu, Phys. Rev. E **81**, 031904 (2010).
[37] P. Bagchi and R. M. Kalluri, Phys. Rev. E **80**, 016307 (2009).
[38] U. Seifert, K. Berndl, and R. Lipowsky, Phys. Rev. A **44**, 1182 (1991).
[39] V. Kantsler, E. Segre, and V. Steinberg, Phys. Rev. Lett. **99**, 178102 (2007).